Proximity proteomics reveals a co-evolved LRRK2-regulatory network linked to centrosomes

Marita Eckert[1,4,5], Pasquale Miglionico[2,5], Francesca Izzi[1], Natalia De Oliveira Rosa[2], Marius Ueffing[3], Francesco Raimondi[2*] and Christian Johannes Gloeckner[1,3*]

[1]German Center for Neurodegenerative Diseases, 72076 Tübingen, Germany;

[2]Laboratorio di Biologia Bio@SNS Scuola Normale Superiore, 56126 Pisa, Italy;

[3]Center for Ophthalmology, Institute for Ophthalmic Research, University of Tübingen, 72076 Tübingen, Germany

[4] Graduate School of Cellular and Molecular Neuroscience, University of Tübingen, 72074 Tübingen, Germany.

[5]contributed equally to this work.

Corresponding authors:

Christian Johannes Gloeckner (johannes.gloeckner@dzne.de)

Francesco Raimondi (francesco.raimondi@sns.it)

Abstract

The Leucine-rich repeat kinase 2 (LRRK2) not only plays a vital role in familial forms of Parkinson's disease (PD) but is also considered as a risk factor for idiopathic PD. Its multi-domain architecture enables a fine-tuned regulation of its biological function by orchestrating intra- and inter-molecular interactions. Here, we present BioID proximity proteomes of LRRK2 revealing new interactors, which we further characterized by a novel evolutionary and structural bioinformatics pipeline. Co-evolutionary analysis of the protein-protein interaction network identified a structural and functional module enriched in cytoskeletal components linked to the centrosome and microtubules. Furthermore, structural modelling of binary interactions via AlphaFold-multimer revealed distinct groups of interactors engaging with LRRK2 dependent on specific conformations and epitopes. Furthermore, we identified distinct changes in the LRRK2 proximity proteome induced by the type I kinase inhibitor MLi-2 or by co-expression of the LRRK2 upstream effector RAB29. Dependent on its state of activity and conformation, these protein-protein interactions link LRRK2 to defined cellular sub-compartments, including centriolar satellites as well as vesicular sub-compartments.

Introduction

Parkinson's disease (PD) is the second most common neurodegenerative disease after Alzheimer's, it occurs mostly sporadically and is distributed with high frequency in the older generations. PD is characterized by a loss of dopaminergic neurons in the *substantia nigra* leading to the motor symptoms associated with the disease (Fahn, 2003). Several therapies targeting the symptoms, such as dopamine substitution, are practiced but so far, no causative therapy exists. About 5-10% of PD cases are inheritable (Gasser et al., 2011). *LRRK2*, localized within the PARK8 locus and coding for the Leucine-rich repeat kinase 2, is one of the genes associated with familial forms of the disease but also represents a risk factor in idiopathic PD (Paisan-Ruiz et al., 2004; Simon-Sanchez et al., 2009; Zimprich et al., 2004). The multi-domain protein LRRK2 is an active protein kinase and, at least, mutations with confirmed disease segregation, including the most common G2019S variant within its kinase domain, augment its kinase activity (Kalogeropulou et al., 2022). This makes LRRK2 an important drug target (Kluss et al., 2022b). ATP-competitive LRRK2-specific kinase inhibitors for PD-treatment are under development and in clinical trials (Jennings et al., 2022). Nevertheless, structural changes of the lung seen in non-human primates indicate a considerable small therapeutic window and additionally challenge a long-term treatment with these compounds necessary to allow a life-long reduction of augmented LRRK2 pathway activation (Miller et al., 2023). For this reason, the identification of alternative drug targets within the LRRK2-associated pathways would be a potential solution for a better control of pathophysiological alterations associated with pathogenic forms of this protein, minimizing the risk of drug-induced lung pathologies. In addition, a larger group of patients beyond LRRK2 mutation carriers might benefit from targeting more common PD-associated pathways.

Various functional studies have demonstrated a function of LRRK2 in vesicle trafficking, including presynaptic vesicles as well as autophagy and lysosomal pathways ((Piccoli et al., 2011); reviewed in: (Follett and Farrer, 2021)). In agreement with these cellular functions, LRRK2 phosphorylates a subset of Rab proteins, small G-proteins involved in vesicular transport, such as Rab8a and Rab10, which is elevated by PD-associated LRRK2 variants (Steger et al., 2017).

In common with other Roco proteins, LRRK2 features a remarkable complexity (Wauters et al., 2019). In fact, LRRK2 contains multiple scaffolding domains, not only being involved in keeping inactive LRRK2 in an auto-inhibited state, as recently demonstrated by high-resolution structures of LRRK2 (Deniston et al., 2020; Myasnikov et al., 2021), but are also involved in protein-protein interactions making LRRK2 a signaling hub possibly integrating multiple up- and down-stream signals (reviewed in: (Manzoni et al., 2015)). These studies suggest that the Roco protein LRRK2 is a tightly controlled protein kinase serving as hub and signal integrator and is most likely involved in context-specific, spatially controlled cellular responses that appear evolutionarily conserved. Quite some effort has therefore been spent on the investigation of the protein-protein interaction networks of LRRK2, mainly by using affinity-

65 based methods. Data of various studies were curated in public databases such as IntAct or STRING and
66 were also subject to meta-analysis to dissect functional LRRK2 signaling networks (Gloeckner and
67 Porras, 2020; Manzoni et al., 2015; Zhao et al., 2024; Zhao et al., 2023). However, affinity-based
68 methods face limits, given their bias for rather stable complexes which miss dynamic/ transient
69 interactions. We therefore used the BioID proximity labeling method to detect new interaction
70 partners of LRRK2. By systematically applying the BioID approach with three different BioID tags, we
71 describe the proximity proteome of LRRK2 under basal conditions. In addition, by a newly designed
72 bioinformatics workflow that estimates co-evolution of interacting partners based on their co-
73 presence in sequenced genomes, we could demonstrate that the resulting BioID datasets are
74 characterized by higher co-evolution values similarly to confirmed direct interactions. Through this
75 approach, we have identified a cluster of interactors featuring a high degree of co-evolution to LRRK2
76 which is enriched in cytoskeletal proteins involved in centrosomal and ciliary dynamics. We predicted
77 the 3D complexes mediated by LRRK2 via AF-multimer, which also revealed distinct conformations and
78 interfaces associated to specific processes. Finally, to further stratify the interactome of LRRK2, we
79 looked at experimentally-defined conformational states of LRRK2, e.g. by investigating the context-
80 specific proximity proteome upon co-expression of the LRRK2 upstream effector RAB29 and upon
81 stabilization of an active-like kinase conformation by inhibition of LRRK2 with a type I ATP-competitive
82 inhibitor (Taylor et al., 2020; Wauters et al., 2019). Inhibition of LRRK2 with the type I inhibitor MLi-2
83 but not with the type II inhibitor GZD-824 lead to an enrichment of a highly specific sub interactome
84 associated with centriolar satellites.

85

86 **Methods**

87 ***Cloning and generation of the stable miniTurbo-LRRK2 cell line***

88 All used proximity tags have been ordered as synthetic genes (Eurofins) and subcloned via *Eco*RI and
89 *Xho*I into pcDNA3.0 (Invitrogen) allowing the expression of fusion proteins in mammalian cells under
90 the strong viral CMV promoter. Gateway Destination clones were generated by cloning a Gateway
91 cassette (Invitrogen) into an *Eco*RV site at the 3' end and in frame of the different BioID-tags [BioID
92 (Roux et al., 2012) (referred as BioID1), BioID2 (Kim et al., 2016), miniTurbo (Branon et al., 2018)]. For
93 better and comparable detection of the fusion proteins, all tags contained an N-terminal HA-tag. The
94 LRRK2 expression clones were subsequently generated by LR cloning (Invitrogen) based on ENTRY
95 clones described earlier (Gloeckner et al., 2010). The CDS of human of RAB29 has been ordered as
96 synthetic gene strand (Eurofins) with flanking attB sites to allow its direct cloning into pDONR201 by
97 BP cloning and subsequently cloned into an in-house (N)FLAG-HA Gateway destination clone by the LR

98 reaction. The HEK293 cell line (ACC-305) stably expressing miniTurbo-LRRK2 has been generated as
99 previously described (Gloeckner et al., 2007). Briefly, single colonies have been selected and tested
100 after transient transfection and selection via G418 (Sigma). The Flag-HA-CYLD vector was kindly
101 provided by Wade Harper (plasmid #22544, Addgene) (Sowa et al., 2009), the pCMV poly HA-ubiquitin
102 construct was kindly provided by D. Bohmann (Treier et al., 1994) and the pRK5-HA-Ubiquitin-K63
103 vector was kindly provided by T. Dawson (plasmid #17606, Addgene) (Lim et al., 2005).

104 ***Cell culture and proximity labelling***

105 HEK239T (ACC-635) or HEK293 stably expressing miniTurbo-LRRK2 were grown in 14cm dishes in full
106 Dulbecco's modified medium (DMEM) supplemented with penicillin streptomycin and if not
107 mentioned otherwise with 10% FBS at 37°C in 5% CO2. The cells were grown for 8 hrs to 1 day reaching
108 a density of 50-80% until transfection with a self-made PEI (Polyethylenimine) reagent (Guaitoli et al.,
109 2016). For each condition, 4-6 plates have been used. If not stated otherwise, for biotinylation, cells
110 have been incubated with 50µM biotin (Sigma) in serum-free medium for up to 16 hours. In case of
111 the mini turbo tag, cells have been incubated with 50 µM biotin for 2h after o/n starvation. Starvation
112 was used to synchronize the cells and, in light of the physiological functions of LRRK2, to enrich for
113 post-mitotic states in which its centrosomal and ciliary roles are more prominent. For the
114 determination of the LRRK2-inhibitor dependent proximity proteomes, a HEK293 line stably expressing
115 mT-LRRK2 was either incubated with 1µM MLi-2, 1µM GZD-824 or DMSO (vehicle) 1h prior and during
116 2hrs biotin incubation. For the analysis of RAB29-dependent proximity proteomes, mT-LRRK2 was
117 either co-expressed with HA-RAB29 or an empty pcDNA3.0 vector. See also the point-to-point protocol
118 deposited on Zenodo (DOI: 10.5281/zenodo.17045153).

119 ***Affinity purification of biotinylated proteins***

120 For cell lysis, cell culture dishes were transferred to ice and culture media was removed. The cells were
121 rinsed two times with 5ml ice-cold PBS. The cells were covered with 1ml lysis buffer [0.5% Nonidet P-
122 40 Substitute (Merck), protease inhibitor cocktail (Roche), PhosSTOP (Roche) in TBS (30mM Tris-HCl,
123 pH7.4 and 150mM NaCl)] per 14cm dish and detached with a cell scraper. The cell suspension was
124 collected and incubated for 20-40min on an end-over-end shaker at 4°C. Lysate were cleared by
125 centrifugation (15,000xg for 10min at 4°C). The protein concentration of cleared lysates was
126 determined photometrically using a nanodrop (Thermo-Fisher Scientific) or with the BCA assay
127 (Thermo-Fisher Scientific) following the manufacturer's instructions. Biotinylated proteins were
128 purified by affinity enrichment using either Strep-Tactin Superflow resin (IBA) or MagStrep Strep-Tactin
129 beads (IBA) in case of small-scale enrichments. To this end, the combined lysates for each condition
130 were incubated with an adjusted resin volume of 25µl packed beads per 14cm cell culture dish. The

131 resin was equilibrated by washing 3-4x with 500µl lysis buffer. The lysates were incubated with the
132 resin overnight at 4°C under constant agitation. The resin was sedimented by centrifugation at 5,000xg
133 for 3min at 4°C, transferred to microSpin columns (Cytiva) and subsequently washed 3x in 500µl lysis
134 buffer followed by two washes in 500µl 1x TBS. Biotinylated proteins were eluted by incubation with
135 300-400µl desthiobiotin elution buffer (2.5M, IBA). The desthiobiotin eluates were precipitated by
136 chloroform/ methanol and directly subjected to tryptic proteolysis following standard protocols
137 (Gloeckner et al., 2009) and stored at -80°C. The BioID protocol was constantly improved during the
138 work. See also the point-to-point protocol deposited on Zenodo (DOI: 10.5281/zenodo.17045153).

139 ***CYLD co-expression experiment***

140 For the analysis of CYLD co-expression, cells were co-transfected with either Strep/FLAG (SF-TAP)
141 tagged LRRK2 WT or LRRK2 Y1699C, CYLD, and ubiquitin (either in WT form or K63) plasmids. As
142 negative control, CYLD plasmid was replaced by pCDNA3 empty vector, to maintain the plasmid
143 concentration constant among the different conditions. For 6-wells, a total of 500ng of plasmid DNA
144 was used for each well; for 14cm plates, a total of 8µg of plasmid DNA was used for each plate. The
145 plasmids ratios were LRRK2:CYLD:Ubiquitin 1:3:1. Transfection and cell lysis were performed as
146 described above.

147 ***siRNA knockdown***

148 24h after splitting, cells were transfected with RNAiMAX (Life Technologies) following manufacturer's
149 instructions. The following siRNAs were used (Silencer Select®, Life Technologies): PCM1 (#s10128,
150 CAAAGACUCCACAUACGUUtt), Negative Control No. 2 (#4390846). 360pmol of siRNA were used for
151 each technical replicate. Cells were kept in culture for another 48h before proceeding with treatment
152 with 10µM MLi-2 or DMSO. Cells were lysed as described above. Three technical replicates for each
153 condition (PCM1 or scrambled, MLi-2 or DMSO) were used. The effects of PCM1 knockdown were
154 evaluated via SDS-PAGE and Western Blot. For each replicate, each individual protein was normalized
155 against total biotinylation. Statistical analysis was performed using GraphPad Prism 10.2.3. Unpaired
156 two-tailed t-tests were used to compare group means; each protein of interest was normalized against
157 total biotinylation.

158 ***SDS PAGE and Western Blots***

159 For functional evaluation of the bait proteins and to determine the biotinylation efficiency, samples
160 were subjected to SDS PAGE and analyzed by Western-blotting on PVDF membranes. To assess blotting
161 efficiency and equal loading, the membranes were stained with Ponceau S. Prior to blocking of the
162 membranes in 5% nonfat dry milk powder (BioRad) or 1-5% BSA (Carl Roth) in TBS with 0.1% Tween 20
163 (TBST) for 1-3h at RT, membranes were de-stained in TBST. Membranes were afterwards incubated

164 with primary antibody solutions overnight at 4°C under mild agitation. The following primary
165 antibodies were used: rat α-LRRK2 mAb (24D8 clone, hybridoma supernatant, generated in house
166 (Carrion et al., 2017)) 1:1000 in 5% milk in TBST), rabbit α-pS935-LRRK2 mAb (Abcam, ab133450;
167 1:100,000 in 5% BSA in TBST), rabbit α-RAB10 mAb (Abcam, ab181367; 1:5,000 in 5% milk in TBST),
168 rabbit α-pT73-RAB10 mAb (Abcam, ab230261; 1:1,000 in 5% BSA in TBST), rat α-HA-tag (Roche, 3F10
169 clone, Rat 1gG1; 1:1,000 in 5% milk in TBST), mouse α-FLAG-tag (Sigma, F1804-200UG, 1:2,000 in 5%
170 milk in TBST), rabbit α-PCM1 (Proteintech, 19856-1-AP, 1:24,000 in 5% milk in TBST), mouse α-CYLD
171 (Proteintech, 66858-1-Ig, 1:1,500 in 5% milk in TBST), rabbit α-SSX2IP (Thermo Fisher Scientific, PA5-
172 31495, 1:1,000 in 5% milk in TBST). Membranes were washed 5x 5min in TBST prior to incubation with
173 the HRP-conjugated secondary antibodies α-rat (Jackson Immuno-Research, 112-036-062; 1:7,500), α-
174 rabbit (Jackson Immuno-Research, 111-036-045; 1:7,500), and α-mouse (Jackson Immuno-Research,
175 115-036-062; 1:7,500), respectively. For the detection of biotinylated proteins, membranes were
176 incubated with Pierce™ High Sensitivity Streptavidin-HRP (Thermo Fisher Scientific, 1:20,000 in 1% BSA
177 in TBST) overnight at 4°C and washed the next day 5x 5min in TBST. Blots were developed with Pierce
178 ECL Plus Western Blotting Substrate following the manufacturer's protocol (Thermo Fisher Scientific)
179 and exposed to Amersham Hyperfilm™ ECL (Cytiva). For quantification of LRRK2 in presence of CYLD,
180 the JESS capillary Western system (Bio-Techne) was used. Data analysis was performed with the vendor
181 software (Compass for SW, v7.0.0) and GraphPad Prism 10.2.3 Unpaired two-tailed t-tests were used
182 to compare group means; each protein of interest was normalized against beta-actin.

183 ***Mass spectrometry***

184 In solution proteolysis was performed as previously described (Gloeckner et al., 2009). Briefly,
185 chloroform/ methanol precipitates were dissolved in 50mM ammonium bicarbonate pH8.0. Cysteines
186 were reduced and alkylated by treatment with 100mM DTT and 300mM Iodoacetamide, respectively
187 following the incubation with trypsin (Sigma-Aldrich) overnight at 37°C. Samples were desalted by
188 micropipette C-18 solid-phase extraction tips (StageTip, Thermo Fisher Scientific) prior to LC-MSMS
189 analysis. Peptides were subsequently analyzed by LC-MSMS using a nanoflow HPLC system (Ultimate
190 3000 RSLC; Thermo-Fisher Scientific) coupled to an Orbitrap Q-Exactive plus (Thermo Fisher Scientific)
191 tandem mass spectrometer. Peptides were separated by reversed C-18 chromatography and 120-
192 minute gradients. MS1 spectra were acquired in the Orbitrap at 70K resolution. After selection of the
193 10 most intense precursor ions from the MS1 scans for HCD fragmentation (Top 10 method), MS2
194 spectra were acquired at 17.5K. RAW MS files were analyzed with Maxquant (version 2.0.3.1), enabling
195 label-free-quantification (LFQ with no normalization) and "match between runs" (Cox et al., 2014). For
196 the embedded Andromeda search engine, trypsin has been selected as enzyme and carbamylation was
197 set as fixed modification N-terminal acetylation was set as variable modification. The search was

198 performed against the human subset of the Uniprot/Swissprot database (release 2021_04, 20375
199 entries). The MaxQuant output was further processed by Perseus and SaintExpress.

200 ***Perseus post-processing***

201 For post-analysis, the protein groups were further processed by Perseus (v. 1.6.7). LFQ intensities of
202 the individual were assigned to the conditions and potential contaminants, reverse hits as well as IDs
203 only identified by site were filtered out. For further analysis, only IDs with a maximum number of
204 missing values of n-1 in at least one condition were considered. Remaining missing values were
205 replaced by group-wise imputation based on a normal distribution (log2 values) around the detection
206 limit (width=0.3; down-shift=1.8). Intensities of the individual experiments were normalized by their
207 medians and significantly enriched proteins (condition vs control) were determined by a T-test
208 combined with an FDR filter (p=0.05, S0=0.1).

209 ***SaintExpress post-processing***

210 We followed a previously described protocol (http://proteomics.fi (Liu et al., 2020)) to select the most
211 confident interactors using the statistical framework of SAINTExpress (Teo et al., 2014), as well as a
212 reference knowledgebase for contaminants (i.e. CRAPome (Mellacheruvu et al., 2013)), to filter out
213 most likely false negative interactors. In particular, we generated the "Bait", "Prey" and "Interaction"
214 files to be subjected to the analysis pipeline from the MaxQuant "*proteinGroups.txt*" file by employing
215 the following columns: "Bait" file (IP name=EV_* or LRRK2_*, bait name=LRRK2, indicator for test and
216 negative control= C=EV_* ;T=LRRK2_*); "Interaction" file (IP name = EV_*/LRRK_*, bait name=LRRK2,
217 prey name=interaction partner gene symbol, spectral count or intensity values=LFQ intensity); "Prey"
218 file (prey (protein)name= interaction partner Uniprot accession, prey protein length=Sequence length,
219 prey gene name= gene symbol). The proteins that were not classified through the CRAPome filter,
220 were retained together with those passing the filter.

221 We unified the interactor list from the three BioID experiments. Finally, we retained a list of 208
222 interactors which passed the two filters. Only 45 proteins in the filtered interactor list are already
223 present in IntAct.

224 ***Graphical representation and network annotation***

225 PPI networks were analyzed by Cytoscape version 3.8.2 (Shannon et al., 2003) and were mapped to
226 available interaction from IntAct using the Cytoscape IntAct app (Ragueneau et al., 2021). Networks
227 were annotated with STRINGDB terms via the 'Stringify' function of the StringApp (Doncheva et al.,
228 2019) and functional enrichment retrieved via the same app. We annotated the networks with the
229 AutoAnnotate plug-in (Kucera et al., 2016), using the GLay clustering method, and generated the

230 cluster labels with the Adjacent Words option of the WordCloud algorithm, based on significantly
231 enriched GO Biological Process and Cellular Component terms associated with the genes in each
232 network. The Venn diagram shown in Figure 1A has been generated with JVenn provided by the
233 ProteoRE server (Galaxy Version 2021.05.12) (Galaxy, 2024).

234 **Co-evolution based PPI stratification**

235 Co-evolution of two proteins A and B was measured as the Jaccard similarity coefficient of the set of
236 genomes containing an orthologous sequence of A and the set of genomes containing an orthologous
237 sequence of B. Orthologous sequences were collected from the Orthologous MAtrix (OMA) database
238 (Altenhoff et al., 2021) using a Python script written in-house using the PyOMADB client (Kaleb et al.,
239 2019) (Kaleb et al., 2019) (December 13, 2023, database version July 2023).

240 **AF-multimer prediction of binary interactions**

241 We used Alphafold-Multimer v2.3.2 (Evans et al., 2021) to generate 3D models of full-length LRRK2
242 binary interaction complexes for all the interactors shorter than 2000 residues. The databases required
243 to run AlphaFold-Multimer were downloaded on 12 January 2023 and the predictions were run with
244 the flag –max template date=01-01-1900, to avoid the usage of any available experimental templates.
245 Among the 5 models generated for each LRRK2 binary complex, only the best one was considered for
246 further analysis. The score used to evaluate the models was the default one used by AlphaFold-
247 Multimer (0.2*pTM + 0.8*ipTM).

248 **Interaction fingerprint**

249 AlphaFold produces probabilities for the $C_ß$-$C_ß$ distances between residues *i* and *j* to fall into a series of
250 distance bins. For each pair of residues, we calculated the expected value of such distance distribution,
251 yielding a matrix of dimension l_{LRRK2} x l_n, corresponding to the sequence lengths of LRRK2 and the *n*th
252 interacting partner, respectively. Subsequently, we pooled the distogram on the interaction partner's
253 side and we assigned to each residue of LRRK2 the minimum expected distance to any residue of the
254 interactor. We refer to this vector of minimum expected distances as the interaction fingerprint of a
255 given interacting protein.

256 **RMSD calculation**

257 We compared LRRK2 conformations by performing Root Mean Square Deviation (RMSD)-based
258 clustering. To calculate the RMSD we fitted the structures using the C_α atoms of the LRRK2 chains from
259 position 983 to the end of the sequence. The N-terminal portion of the protein was excluded because
260 it is very flexible. Calculations were performed using the Superimposer function of the PDB Biopython
261 module (Cock et al., 2009) (version 1.83) through customized scripts and pipeline (Matic et al., 2023).

262

263 **Clustering**

264 The clustering was performed using the Ward method with the *clustermap* function from *seaborn*
265 python library (version 0.11.2). Results were displayed through matplotlib (https://matplotlib.org/)
266 and seaborn (https://seaborn.pydata.org/) libraries using customized python scripts. The number of
267 clusters chosen was one that maximized the mean Silhouette Coefficient of all samples (Rousseeuw,
268 1987) , as computed by the *silhouette_score* function in *scikit-learn* (Pedregosa et al., 2011).

269

270 **Results**

271 *Definition of cellular LRRK2 proximity proteomes with BioID1, BioID2 and miniTurbo.*

272 The elucidation of comprehensive protein-protein networks represents a powerful tool not only to
273 identify signaling pathways associated with a protein of interest but also to connect different
274 pathogenic mutations in a disease network or identify novel disease-associated proteins through
275 proximity to known proteins (Boldt et al., 2016; Kiel et al., 2011). This approach might ultimately lead
276 to the discovery of new drug targets as well as disease biomarkers. For this reason, various studies
277 addressed the interactomic networks of LRRK2 in a different cellular context or model organism (Islam
278 et al., 2016; Meixner et al., 2011; Piccoli et al., 2011; Piccoli et al., 2014). However, most of the used
279 technologies rely on immuno-precipitation or pull-downs, which have a bias for considerable stable
280 PPIs while transient interactions remain underrepresented. In the last years, proximity-based
281 methods, e.g. BioID, have been developed allowing the identification of PPIs under physiological
282 conditions and within cells also covering transient interactions. The BioID approach is based on a
283 variant of the bacterial biotin ligase BirA, which has been converted to a promiscuous labeling tool by
284 a single point mutation within its active center allowing the release of the reactive intermediate
285 biotinyl-AMP. To determine the LRRK2 proximity proteome, we have generated different N-terminal
286 fusion proteins. Besides the original BioID (BioID1) tag (Roux et al., 2012), we used the BioID2 (Kim et
287 al., 2016) as well as miniTurbo, a shorter version of the TurboID tag, lacking the BirA DNA binding
288 domain (Branon et al., 2018). For reasons of comparability, all tags have been cloned in the same way,
289 containing an N-terminal HA tag for detection and a 3x(GGGS) linker between the tag and the protein
290 of interest inserted C-terminally of the tag by Gateway-cloning. All constructs were functionally
291 assessed to demonstrate biotinylation activity and to ensure the tag does not interfere with the activity
292 of LRRK2. Western blot analysis shown in Supplemental Figure 1 demonstrates that all constructs
293 allowed sufficient biotinylation in cells. As expected, BioID2 and miniTurbo showed a higher labeling
294 efficiency compared to BioID1. We also confirmed that the fusion proteins are still able to
295 phosphorylate the physiological LRRK2 substrates by probing for Rab10 phosphorylated on Threonine-
296 73 (see: Supplemental Figure 1).

297 After initial functional tests, all three fusion constructs were used to determine their interactomes
298 after transient expression in HEK293T cells. To increase the stringency of the approach, a tag-only
299 control (corresponding BioID tag) was used as reference. For the relative comparison of the LRRK2 vs.
300 the tag-only control, the expression levels were adjusted via pre-experiments and always confirmed
301 by Western blot analysis of the cell lysates. In contrast to comparing plus/minus biotin conditions, the
302 tag-only control allows to efficiently exclude natively biotinylated proteins as their degree of
303 biotinylation is also increased by the biotin treatment of the cells already by the experimental design.
304 The data of all three proximity proteomes were analyzed by SaintExpress and, alternatively, by
305 labelfree quantification (LFQ) combined with an FDR-controlled T-test as implemented in Perseus
306 (Tyanova et al., 2016). To further filter and analyze the data set, we implemented a bioinformatics
307 pipeline based on interacting genes co-evolution and structural modeling by Alphafold-Multimer
308 (Figure 1A). With BioID1, BioID2 and miniTurbo, 168, 312 and 241 proteins were identified,
309 respectively, as being significantly enriched in the LRRK2-containing condition over the tag-only control
310 by the LFQ approach (Figure 1B; Table S1). SaintExpress (Teo et al., 2014) and subsequent filtering
311 against the Crapome data of commonly found false-positive hits (Mellacheruvu et al., 2013), however,
312 appeared to be the more stringent analysis compared to MS1-based label-free quantification. Based
313 on this analysis, we created a non-redundant set of 208 unique interactors, hereinafter referred to as
314 "BioID set" which was submitted to the bioinformatics post-processing pipeline.

315 *Functional-enrichment analysis of the LRRK2 proximity proteome*

316 We compared the LRRK2 BioID interactome with a reference LRRK2 interactome available from IntAct
317 (Orchard et al., 2014). We found that only 54 interactors in the filtered BioID set were previously
318 reported in association with LRRK2, while the vast majority (154) were not yet reported for their
319 interaction with LRRK2 (Figure 2A,B). By integrating the LRRK2 BioID interactome with the network of
320 known interactions from Intact it is possible to define several modules of proteins interacting with
321 each other in addition to LRRK2 (Figure 2A). Among the enriched intracellular and cytosolic
322 compartment, we found terms related to microtubules (e.g. Microtubule Cytoskeleton, FDR=5.83E-15)
323 and Centrosome (FDR= 1.43E-13), emphasizing the importance of LRRK2 in microtubule organization
324 (Figure 2C) and representing the largest module of interacting proteins in the network (Figure 2A). In
325 addition, we also found processes related to cell cycle and mitosis (e.g. "Regulation of mitotic cell
326 cycle", FDR=9.71E-08) (Figure 2D).
327 Multiple protein domains instances are significantly enriched within the list of identified LRRK2
328 interaction partners (Figure 2E). In particular, we found that the Armadillo-type fold instance is the
329 most enriched one (FDR= 9.58E-06), which is found in 21 distinct interactors, followed by other
330 domains with lower, but still significant, degree of enrichment, such as "Forkhead-associated (FHA)

331 domain" (Almawi et al., 2017), found in six distinct proteins, the "DIX domain" (Ehebauer and Arias,
332 2009; Kafka et al., 2014) found in four proteins, the "K Homology domain, type 1" (Grishin, 2001) found
333 in six proteins and "Ubiquitin-like domain superfamily" (FDR<0.05), the latter being found in 11 distinct
334 interacting proteins. Interestingly, LRRK2 and its Drosophila orthologue dLRRK have been
335 demonstrated to functionally interact with the Forkhead box transcription factor FoxO1/dFoxO. In
336 particular, LRRK2-mediated phosphorylation of FoxO1 enhances its transcriptional activity leading to
337 neuronal toxicity (Kanao et al., 2010).

338 *Analysis of co-evolution reveals a cluster of proteins involved in centrosome/ microtubular dynamics*

339 We analyzed the extent of co-evolution of LRRK2 with its interactors to prioritize the most conserved
340 relationships associated to LRRK2's functions. We derived a metric for the co-evolution between two
341 interacting proteins based on the degree of co-presence, assessed through a Jaccard score, of
342 interacting gene pairs in sequenced genomes available from a reference orthology database (e.g. OMA,
343 see Methods). We found that such simple co-evolutionary metric is informative about non-enzymatic,
344 direct interactions as well as stable complexes at a human interactome-wide level (Meldal et al., 2022;
345 Miglionico et al., 2024; Orchard et al., 2014) (Table S2A). We found similar trends when focusing on
346 LRRK2 interactions reported in IntAct, with "non-enzymatic direct" PPIs being characterized by a
347 significantly higher Jaccard score compared to those categorized as "association" or "physical
348 interaction" (Figure 3A). Intriguingly, we found that the distribution of co-evolution metrics calculated
349 for BioID interactors is significantly higher than most IntAct categories (i.e. "association", "physical",
350 "enzymatic direct") and it is as high as the non-enzymatic direct interactions (Figure 3A). This result
351 suggests that interactors captured within the BioID dataset are more likely to represent stable, direct
352 interaction partners of LRRK2 with whom they co-evolved. Likewise, simple co-evolution scores are
353 predictive for LRRK2 direct interactions, particularly the non-enzymatic direct ones (Figure 3B; ROC
354 AUC=0.715). In the case of the LRRK2 interactome, we found that this co-evolutionary metric is more
355 predictive of non-enzymatic direct interaction compared to another co-evolution estimate, i.e. Mutual
356 Information (ROC AUC=0.66; Supplemental Figure 2), which is instead more predictive at a human
357 proteome scale (Miglionico et al., 2024).
358 We used the co-evolution metric to cluster LRRK2 and its interactors, which revealed groups of proteins
359 characterized by reciprocal high co-evolution (Figure 3C). The different groups of interactors are also
360 characterized by specific biological processes, which are overall mutual exclusive to each other,
361 suggesting that clusters of co-evolved proteins underpin specific functional interactions and biological
362 processes (Supplemental Figure 3). Notably, the cluster containing LRRK2 (i.e. Cluster 2) is
363 characterized by on average higher co-evolution and several highly co-evolved proteins (Figure 3C).
364 The top 10 proteins of Cluster 2 showing highest co-evolution are summarized in Table 1. By mapping

365 members of this cluster onto the STRING functional interaction network (Figure 3D, see Methods), we
366 found functional interactions for most of the members, including LRRK2. Overall, STRING yielded a
367 highly significant PPI enrichment (P-value=1.0E-16), suggesting that these proteins are more likely to
368 interact with themselves than with randomly selected proteins. Moreover, network topology analysis
369 delineated two distinct submodules: the first encompassing LRRK2 together with proteins
370 predominantly linked to Wnt signaling (FDR = 0.0013; Figure 3E), and the second consisting of proteins
371 implicated in cytoskeletal processes ("Protein localization to microtubule cytoskeleton"; FDR=2.18E-
372 05), centrosome dynamics ("Loss of Nlp from mitotic centrosomes"; FDR = 0.00086) and centriole
373 organization ("Centriole"; FDR = 1.11E-05). Consistently, Cluster 2 displayed strong enrichment for
374 cellular component terms, most notably "Microtubule Cytoskeleton" (FDR=2.10E-12) and
375 "Centrosome" (FDR=1.01E-12) (Table S2B). Interestingly, the single most co-evolved protein to LRRK2
376 is CYLD, a deubiquitinase that acts as a negative regulator of dopamine neuron survival in Parkinson's
377 disease (Pirooznia et al., 2022), but that has not yet been reported in direct interaction with LRRK2.
378 Interestingly, CYLD emerges as a critical bridging element that connects the two principal submodules
379 within Cluster 2's interactome (Figure 3D).
380 On the other hand, Cluster 1 is characterized by distinct processes, such as FAR/SIN/STRIPAK complex
381 (P-value= 0.0012; Table S2B). Taken together, these results suggest that our co-evolution-based
382 approach was able to identify a group of LRRK2 interacting proteins, mostly associated to microtubule
383 and centrosome functions via the formation of stable, supramolecular complexes.
384 Likewise, co-evolution-based clustering of LRRK2 interactors from IntAct shows interactors such as
385 RAB29, RAB12, LRRK1 or SNCA among the most co-evolved partners which clustered with LRRK2
386 (Supplemental Figure 4), confirming the tight evolutionary constraint on LRRK2's functional regulation.

387 After confirming the proximity of LRRK2 and CYLD (Figure 3F) by Western blot, we investigated the
388 functional relevance of the interaction between LRRK2 and CYLD by examining whether the latter
389 influences the stability of the former. Notably, co-expression of CYLD led to a marked increase in LRRK2
390 stability. This effect was observed for both wild-type LRRK2 and the pathogenic Y1999C variant, which
391 is characterized by elevated Rab phosphorylation levels but reduced protein stability, as quantified
392 using capillary-based Western blotting (Figure 3G-H). Given that CYLD is a deubiquitinase with
393 specificity for K63-linked ubiquitin chains, we co-expressed HA-tagged ubiquitin constructs—one
394 encoding wild-type ubiquitin and another engineered to exclusively support K63-linked
395 polyubiquitination (with all other lysines mutated to arginine, as described by Kaleb et al. (Kaleb et al.,
396 2019)). Consistent with CYLD's known substrate specificity, the stabilizing effect on LRRK2 was
397 significantly enhanced, while only a trend was observed with wild-type ubiquitin. A second,
398 independently conducted biological replicate confirmed these trends (Supplemental Figure 5).

399 In summary, our data demonstrate that CYLD co-expression enhances LRRK2 protein stability,
400 supporting a functional role for CYLD-mediated deubiquitination in regulating LRRK2 turnover.

401 *AF-based modelling reveals a discrete repertoire of conformations and interfaces shaping the LRRK2*
402 *interactome*

403 We predicted 3D complexes for binary interactions of LRRK2 and 196 partners in the BioID dataset via
404 AlphaFold-multimer (AF) and characterized their interfaces and conformations (Figure 4A).
405 We structurally aligned LRRK2 conformations in the different complexes by superimposing the
406 monomeric LRRK2 chains and then calculating the pairwise distance of all the possible pairs via Root
407 Mean Squared Deviation (RMSD) (Figure 4A; Methods). We performed hierarchical clustering of LRRK2
408 structures based on RMSD, through which we identified two main clusters (Figure 4B). A smaller one
409 is characterized by conformations with lower deviation from the inactive LRRK2 structure (PDB ID:
410 7LHW), which we termed "locked" (Figure 4B-D). The main structural hallmarks characterizing the
411 "locked" conformation and inherited by the experimental inactive LRRK2 structure (PDB:7LHW)
412 (Myasnikov et al., 2021), are the LRR wrapping around the catalytic domains, particularly the kinase,
413 and a contact formed by the extended loop within the LRR repeats, which includes the hinge helix, and
414 the C-terminal WD40 (Myasnikov et al., 2021). A bigger cluster comprised conformations that are
415 characterized by a larger deviation from the inactive structure, due to a major rearrangement of the
416 LRR, ROC and COR domains, which we termed "unlocked" (Figure 4B-D). Such conformations are
417 reminiscent of the ones that we observed in the predicted LRRK2-RAB10 complex, which we validated
418 as the AF-predicted conformation best accommodating experimental XL-MS data (Guaitoli et al.,
419 2023). Intriguingly, we found that proteins interacting with LRRK2 in these two alternative
420 conformations are associated with distinct evolutionary and functional properties. Indeed, LRRK2's
421 complexes in the "locked" conformations are characterized by a significantly lower RMSD (P-
422 value=3.81E-20; Figure 4D) and higher co-evolution (P-value=1.33E-3; Figure 4E) than the complexes
423 in the "unlocked" conformations. The two groups are also characterized by largely exclusively enriched
424 processes (Figure 4F). In particular, the interactors engaging with LRRK2 in the locked conformation
425 are significantly associated with processes linked to centriolar satellites (P-value=4.76E-10) and cilium
426 assembly (P-value= 0.0001) (Figure 4G; Table S2C). Those interacting with the unlocked conformations
427 are associated with a higher number of enriched processes, including cluster-specific ones such as
428 cytoskeleton (P-value= 4.53E-09) or the microtubule organizing center MTOC (P-value= 6.40E-07).
429 Hence, the predicted LRRK2 conformational switch might be relevant in orchestrating the interaction
430 with partners associated with distinct functions.
431 We also explored patterns of engagement of interactors with the different regions of the LRRK2 multi-
432 domain architecture. To this end, we considered the distribution of distance probabilities (i.e.

433 distograms) generated by AF for each binary interaction and mapped the most likely interacting
434 residues of the partners with respect to LRRK2 positions. We used these partner-specific interaction
435 fingerprints to cluster the interactome and identified four major groups of proteins, each named
436 according to the LRRK2 3D interface involved in the interaction (Figure 5A; Table S2D; see Methods).
437 The Core cluster comprises partners that interact with the LRR–ROC–COR–KIN domains and was
438 named accordingly, as these domains represent the most evolutionarily conserved regions of LRRK2
439 (Figure 5A,B). The WD40 cluster includes complexes involving the homonymous domain (Figure 5A,C),
440 while the ARM cluster comprises proteins engaging a newly identified site within the Armadillo domain
441 (Figure 5A,D). Lastly, the "Other" cluster contains proteins with alternative interaction modalities or
442 no clearly defined binding interface (Figure 5A). Complexes predicted to interact with the Core group
443 displayed significantly higher AlphaFold confidence scores compared to those interacting with the
444 WD40 domain (P-value=1.14E-8) or via "Other" interaction modalities (P-value=4.86E-14; Figure 5E).
445 Complexes of the Core group are also characterized by significantly higher RMSD from interactors of
446 the WD40 one (P-value=4.05E-3; Figure 5F), which bind LRRK2 in both locked and unlocked
447 conformations (see below). In the Core cluster we found established LRRK2 interactors, such as DVL1-
448 2, confirming the known interaction mechanism through the ROC-COR domains (Sancho et al., 2009).
449 In the same cluster, we also found novel interactors discovered within the BioID set, such as e.g. CYLD
450 interacting through the Core interface in a similar way. A second cluster displayed higher likelihood of
451 interaction with the WD40 domain (Figure 5A,C), with predicted complexes characterized by a similar
452 interface involving the binding of a short, disordered peptide stretch to a conserved crevice formed by
453 β-propeller loops of the WD40 domain (Figure 5C). WD40 domain binders might bind to LRRK2 in either
454 locked or unlocked conformation (Figure 5A, F), as also suggested by a bi-modal distribution of the
455 LRRK2 chain RMSD (Figure 5F). These interactors also displayed significantly higher co-evolution with
456 respect to "Other" LRRK2 interactors (P-value=5.57E-4; Figure 5G). The ARM cluster involves proteins
457 showing binding preferences for a new docking site on the Armadillo domain, centered around
458 residues 500-600 and mediating the interaction with proteins such as AXIN1 (Figure 5A,D). The larger
459 cluster (Other) contains proteins interacting with weaker likelihood and variable docking sites (Figure
460 5A). Among these, we also found proteins engaging with two more ARM docking sites, including one
461 (around aa 240) which has been recently shown to interact with RAB12 (Dhekne et al., 2023; Li et al.,
462 2024) and mediate a RAB29-independent LRRK2 Kinase activity activation (Purlyte et al., 2018; Zhu et
463 al., 2023), which is predicted to interact with proteins such as KIF16B. A third ARM binding region,
464 encompassing aa 354-444, corresponds to the RAB29 interaction interface found in the recently
465 determined RAB29-bound, tetrameric LRRK2 structure (Zhu et al., 2023), and is the predicted interface
466 for proteins such as NBR1 and MON2.

467 Overall, these results further support the hypothesis that interactors *de-novo* identified by proximity
468 labelling may physically interact with LRRK2 domains through specific conformations and contact
469 interfaces. Interactors lacking a strong interaction probability in the distogram might represent
470 proteins interacting with LRRK2 either transiently or indirectly.

471 *Type I but not type II inhibitors lead to conformational changes directing LRRK2 to centriolar satellites*

472 As mentioned above, LRRK2 adopts multiple conformations through which it engages with its
473 interactors. Effector-mediated oligomerization to an asymmetric tetramer has been demonstrated to
474 switch LRRK2 to an active conformation (Zhu et al., 2023). In addition, ATP-competitive kinase
475 inhibitors can stabilize different conformations. While type I inhibitors stabilize the kinase domain in
476 an active-like conformation, type II inhibitors stabilize the inactive conformation of the kinase domain
477 (Deniston et al., 2020; Raig et al., 2024; Zhu et al., 2024). Interestingly, type I but not type II inhibitors
478 lead to a rapid dephosphorylation of LRRK2 phospho-sites in an interdomain space downstream of the
479 hinge-helix which locks LRRK2 in a compact inactive fold by binding the C-terminal WD40 domain
480 (Kalogeropulou et al., 2022; Myasnikov et al., 2021). We hypothesized that specific inhibitors could
481 distinguish the proximity proteome of LRRK2 in its active versus inactive conformation. To test this, we
482 compared the LRRK2 proximity proteome in HEK293 cells stably expressing miniTurbo-tagged LRRK2
483 following treatment with the type I kinase inhibitor MLi-2, the type II inhibitor GZD-824 (previously
484 shown to inhibit LRRK2 in cells (Kalogeropulou et al., 2022; Tasegian et al., 2021)), or a DMSO control.
485 Western blot analysis of LRRK2 pS935 and pT73-Rab10 confirmed effective inhibition under these
486 conditions (Supplemental Figure 6A). Quantitative label-free analysis combined with an FDR-controlled
487 t-test revealed that only MLi-2 treatment led to the enrichment of a distinct set of proteins associated
488 with cilia assembly and centriolar satellites in the LRRK2 proximity proteome (Figure 6A–E,
489 Supplemental Figure 6B), a pattern not observed with GZD-824. Intriguingly, interactors determined in
490 presence of the MLi-2 inhibitor are characterized by a significantly higher co-evolution (Figure 6F)
491 compared to other BioID interactors. The complete list of significantly enriched proteins (MLi-2 vs.
492 DMSO) is shown in Table 2. Additional information is provided in Table S1.

493 To functionally validate the interaction between LRRK2 and centriolar satellites, we first confirmed
494 that LRRK2 associates with key components of these membrane-less organelles, including the central
495 scaffold protein PCM1 and the centrosome maturation factor SSX2IP (Barenz et al., 2013).
496 Both proteins were enriched in LRRK2 proximity proteomes following biotin treatment, with their
497 interaction further enhanced by the LRRK2 inhibitor MLi-2. To further substantiate LRRK2's association
498 with centriolar satellites, we employed RNA interference to deplete PCM1, a strategy known to disrupt
499 satellite integrity (Dammermann and Merdes, 2002). As expected, PCM1 depletion led to its absence
500 from the LRRK2 proximity proteome and also abolished the association between LRRK2 and SSX2IP.

501 Remarkably, SSX2IP was entirely absent from LRRK2 proteomes regardless of MLi-2 treatment,
502 indicating that LRRK2's interaction with SSX2IP is dependent on intact centriolar satellites. Finally, we
503 asked whether the MLi-2–induced dephosphorylation of serine 935—located near the LRRK2 hinge
504 helix—is affected by satellite disruption. However, PCM1 knock-down did not influence serine 935
505 dephosphorylation, suggesting that this post-translational modification occurs independently of
506 centriolar satellite integrity (Figure 6D, Supplemental Figure 6C).

507 *RAB29 co-expression directs LRRK2 to well established lysosomal protein networks*

508 It has been previously shown that LRRK2 interacts with the RAB29/RAB32/RAB38 family of small G-
509 proteins and subsequently locates to post-Golgi endomembranes (Beilina et al., 2014; McGrath et al.,
510 2021; Vides et al., 2022; Waschbusch et al., 2014). Furthermore, RAB29 not only recruits LRRK2 to
511 lysosomal membranes but also induces its tetramerization (Zhu et al., 2023). For this reason, we
512 performed the BioID experiment in dependence of RAB29 co-expression to determine PPI networks
513 associated with the activated oligomeric state of LRRK2. In addition to mT-LRRK2, either RAB29 or an
514 empty vector were co-expressed. The resulting differential proximity proteome showed differentially
515 enriched proteins only for the condition where RAB29 was co-expressed, demonstrating that a small
516 portion of LRRK2 was recruited by RAB29 with lesser impact on the total proximity proteome (Figure
517 6G). While we did not observe any significant difference in terms of co-evolution of the RAB29
518 differential proteome with respect to the BioID one (Figure 6F), we found significant enrichment in
519 proteins involved in vesicular transport, including the post-Golgi/ lysosomal compartment as revealed
520 by an LFQ analysis combined with an FDR-controlled T-test (Figure 6H,I). In particular, known LRRK2
521 effectors, namely RAB8A (Steger et al., 2017) and SPAG9 (Boecker and Holzbaur, 2021; Bonet-Ponce
522 et al., 2020; Kluss et al., 2022a) were among the enriched proteins (Figure 6G,H). Furthermore, VAMP7,
523 which is part of a SNARE complex mediating autophagosome-lysosome fusion (Jian et al., 2024), was
524 among the significantly enriched proteins (Figure 6G,H). VAMP7-LRRK2 physical interaction has
525 recently been described (Filippini et al., 2023). The complete list of significantly enriched proteins is
526 shown in Table 3. Additional information is provided in Table S1.

527 *MLi-2 and RAB29 differently modulate the shape the LRRK2 interactome*

528 We constructed 3D models of binary complexes between LRRK2 and its partners from the MLi-2– and
529 RAB29-dependent interactomes, and examined both the complex interfaces and the conformational
530 states of LRRK2 (Vides et al., 2022).
531 Interface-based clustering suggests that MLi-2–dependent interactors engage with LRRK2 through
532 specific domain regions, particularly the ones involving terminal domains (Supplemental Figure 7A),
533 while they are predicted to engage little with the catalytic domains, particularly the kinase, which is

534 consistent with the MLi-2 inhibitor function, while in the RAB29-dependent LRRK2 interactome we see
535 a more variable pattern of engaged interfaces. In particular, predictions for this interactome revealed
536 a cluster of proteins interacting with LRRK2 through the ROC-COR-KIN domains, including the RAB8A
537 substrate (Supplemental Figure 7B), suggesting that in the context of RAB29 overexpression several
538 partners might bind in a substrate-like manner. Notably, this interaction modality is absent in the
539 predicted binary complexes of the MLi-2–bound interactome, confirming that the inhibitor prevents
540 LRRK2 from binding substrate-like partners. Moreover, we further validated the capability of the
541 distogram-based interface-fingerprint to discriminate functionally relevant LRRK2 interactors. We
542 predicted the 3D complexes of LRRK2 with known interacting Rabs, and we found out that Rab
543 substrates clustered separately from interacting RABs with distinct functions (e.g. RAB29 and RAB32;
544 Supplemental Figure 7B).
545 From a conformational perspective, we pooled the RAB29- and MLi-2–dependent interactomes and
546 clustered LRRK2 structures based on RMSD, which likewise revealed distinct locked and unlocked
547 clusters. Interactors from the RAB29-dependent interactome are predicted to bind LRRK2 in both
548 conformations, with a particular enrichment in the unlocked state. (Figure 7A). Conversely, MLi-2–
549 dependent interactors were significantly enriched in the locked LRRK2 conformation (Fisher's exact
550 test, P = 0.023), further suggesting that the inhibitor-bound state favors engagement with partners
551 that, unlike substrates, do not require interaction with the kinase domain (Figure 7A). Also for these
552 interactors, the locked conformation has a significantly lower RMSD (P-value=3.85E-6; Figure 7D) and
553 a tendency towards higher co-evolution (Figure 7E). Notably, enrichment analysis of interaction
554 partners grouped by conformational cluster revealed even stronger cluster-specific associations, with
555 only a single process shared between partners in the locked and unlocked conformations (Figure 7F,
556 G; Table S2E).

557

558 **Discussion**

559 The systematic analysis of the interactomes of disease-associated proteins is a powerful tool to dissect
560 molecular networks and to identify pathways relevant for the molecular pathophysiology, for example
561 demonstrated by the comprehensive interactomic network underlying the assembly and homeostasis
562 of primary cilia (Boldt et al., 2016). Given its complex domain structure and tight regulation, LRRK2 is
563 most likely representing a scaffold protein orchestrating distinct signaling complexes, which makes the
564 analysis of its PPI networks an attractive approach to dissect context-specific signaling pathways
565 (Gloeckner and Porras, 2020). While a wealth of data is available for affinity-based identification of
566 protein-protein interactions, which have a bias for rather stable complexes, there is an unmet need
567 for the dissection of less stable and transient PPIs. The rapid development of biotin-based proximity

568 labelling technologies has made it possible to explore previously inaccessible regions of the
569 interactome (Qin et al., 2021). Consequently, APEX and BioID have emerged as widely used techniques
570 for dissecting protein–protein interaction (PPI) networks (Li et al., 2017). For LRRK2, the first APEX2
571 dataset only recently became available recently (Bonet-Ponce et al., 2020). In the present study, we
572 systematically investigated the proximity interactome of LRRK2 using three different BioID tags—
573 BioID1, BioID2 and miniTurbo. The resulting data showed the expected overlap with previously
574 reported interactors, while also uncovering numerous novel candidates. However, several anticipated
575 interactors, including Rab proteins, were not detected in the initial BioID experiments. Nevertheless,
576 Rab8a was identified together with Rab29 upon co-expression of Rab29, which may reflect
577 conformational constraints that reduce accessibility for BioID-mediated biotinylation. Consistent with
578 these observations, a recent comparison of BioID and co-immunoprecipitation in the context of the
579 nuclear pore complex demonstrated that the two approaches provide functionally relevant yet
580 complementary interaction profiles (Moreira et al., 2023).

581 To identify direct LRRK2 interactors with high confidence from the proximity proteomes, we applied a
582 newly developed bioinformatic pipeline relying on co-evolution, co-expression and protein domain
583 architecture to predict interaction type (Miglionico et al., 2024). This pipeline allowed the identification
584 of a group of proteins within the proximity proteome showing a high degree of co-evolution with LRRK2
585 which is highly enriched in proteins associated with the centrosome. This is particularly interesting as
586 pathogenic LRRK2 has previously been shown to lead to a centrosome cohesion defect as well as to a
587 shortening of primary cilia (Dhekne et al., 2018; Khan et al., 2024; Lara Ordonez et al., 2022).
588 Furthermore, defects in primary cilia emerge as a new pathophysiological scheme connecting different
589 genes involved in mendelian forms of Parkinson's disease (Mohd Rafiq et al., 2024; Schmidt et al.,
590 2022). Strikingly, in the cluster of proteins with higher co-evolution to LRRK2 (Cluster 2), the single
591 protein showing the highest co-evolutionary association was the deubiquitinase CYLD. The K-63
592 selective deubiquitinase CYLD is a key effector in the biology of primary cilia. Furthermore, preliminary
593 functional data indicate that CYLD, when co-expressed, is able to increase expression levels of the
594 pathogenic variant LRRK2 Y1699C which shows a decreased protein stability. In fact, this DUB has been
595 shown to control apical docking of basal bodies in ciliated epithelial cells (Eguether et al., 2014). It also
596 regulates centrosomal satellites proteostasis by counteracting the E3 ubiquitin ligase MIB1 (Douanne
597 et al., 2019). Furthermore, CYLD has been shown to deubiquitinate Cep70 and to inactivate HDAC6
598 thereby mediating ciliogenesis (Yang et al., 2014). Interestingly, a missense mutation has recently been
599 shown to be a causative gene for FTD-ALS (Dobson-Stone et al., 2020). Most importantly, as the
600 deubiquitinase CYLD is part of the PINK1/Parkin pathway to regulate cellular levels of PARIS (ZNF746),
601 it is a critical regulator of mitochondrial biogenesis thereby acting as a negative regulator of dopamine
602 neuron survival in Parkinson's disease. In fact, CYLD inhibition has been shown to ameliorate

603 mitochondrial pathologies in cellular PD models which makes CYLD a promising target for therapeutic
604 intervention for PD and other neurodegenerative diseases (Pirooznia et al., 2022). The E3 ligase Parkin
605 preserves mitochondrial homeostasis via the PARIS/PGC-1a axis (Stevens et al., 2015; Zheng et al.,
606 2017). Noteworthy, the PD risk variant LRRK2 G2385R has recently been shown to alter mitochondrial
607 biogenesis via the PGC-1a pathway, leading to reduced PGC-1a levels similarly to a Parkin knock-out in
608 DA neurons (Kumar et al., 2020; Xue et al., 2023). Parkin-deficient DA neurons show increased PARIS
609 and decreased PGC-1a levels (Kumar et al., 2020). In conclusion, this indicates that LRRK2/CYLD
610 signaling, at one hand, and Parkin signaling at the other, might converge on PARIS.

611 The second most co-evolved interactor found in Cluster 2 was the cilia-associated protein CEP85, which
612 plays a role in centrosome disjunction (Chen et al., 2019). This is of particular interest as pathogenic
613 LRRK2 variants lead to a centrosomal cohesion phenotype in patient-derived cells (Lara Ordonez et al.,
614 2019). Notably, the cohesion phenotype is also seen in EBV-transformed lymphoblastoid cell lines from
615 iPD patients which can be reverted by LRRK2 kinase inhibition (Naaldijk et al., 2024). Importantly,
616 Cluster 2 also contains the autophagy cargo protein p62/sequestosome-1. This protein has previously
617 been identified as LRRK2 interactor and substrate (Kalogeropulou et al., 2018; Park et al., 2016).
618 SQSTM1 is also linked to PD pathophysiology via the Pink1/Parkin pathway (Shin et al., 2020). In
619 addition, Cluster 2 points towards other pathways which have been previously linked to PD pathology.
620 In particular, SNAP47 is part of the STX17-SNAP47-VAMP7/8 pathway, which has been shown to be
621 involved in selective autophagy – a process not only essential for the homeostasis of primary cilia but
622 also for mitophagy (Jian et al., 2024). Phospho-ubiquitin chains generated by PINK1/Parkin activity can
623 recruit autophagy adaptors including the ubiquitin adaptor SQSTM1/p62 linking the PINK1/Parkin-
624 dependent pathway to mitophagy (Geisler et al., 2010). All three proteins participate in the
625 recruitment of the autophagy machinery to aged or dysfunctional mitochondria, which are eventually
626 enclosed inside an autophagosome and subjected to the lysosome for degradation (Wilhelm et al.,
627 2022).

628 Interestingly, also the kinesin motor protein and PX-domain containing protein KIF16B was among the
629 top hits which is involved in vesicle trafficking and receptor recycling. It binds to PdIns(3)P by its unique
630 PX domain and promotes the circulating cargo movement from early endosomes to the plasma
631 membrane (Li et al., 2020). Interestingly, it has been found to be associated with lipid droplets
632 (Bersuker et al., 2018). In turn, increased RAB8a phosphorylation by pathogenic LRRK2 variants, has
633 been shown to promote lipid storage (Yu et al., 2018), indicating that the functional interaction of
634 LRRK2 and KIF16B might contribute to alterations in the neuronal lipid homeostasis associated with PD
635 pathology (Hallett et al., 2019).

636 Furthermore, conformational changes induced by MLi-2 binding—leading to rapid and nearly complete
637 dephosphorylation of LRRK2 in a disordered domain downstream of the hinge helix—positioned LRRK2
638 in proximity to a molecular network around PCM1, OFD1, and CEP131, strongly supporting a link
639 between LRRK2 and centriolar satellites. Strikingly, the proteins interacting with LRRK2 in presence of
640 MLi-2 displayed the highest degree of co-evolution, suggesting that the connection between LRRK2
641 and centriolar satellites is highly conserved. The conformational changes induced by binding of type I
642 inhibitors might result in a phase transition of LRRK2 into centriolar satellites preventing 14-3-3 binding
643 and thereby shifting the equilibrium towards the dephosphorylated protein. A similar mechanism has
644 been shown for CEP131, which is extracted from centriolar satellites by phosphorylation and
645 subsequent binding of 14-3-3 (Tollenaere et al., 2015). Centriolar satellites not only play an essential
646 role in the biogenesis of primary cilia (Hall et al., 2023) but also play a role in the degradation of
647 proteins by driving the assembly of aggresomes (Prosser et al., 2022). In fact, also LRRK2 has been
648 shown to interfere with aggresome formation preceding autophagic clearance (Bang et al., 2016).
649 Nevertheless, one caveat might be seen in the fact that LRRK2 inhibition with type I inhibitors induces
650 its destabilization and degradation (Lobbestael et al., 2016).

651 Structural prediction of LRRK2 binary complexes with AF revealed distinct interfaces within each
652 determined interactome. While several interactors preferentially engage with the catalytic core of the
653 protein, including the ROC and KIN domains, others are more likely to interact on terminal domains
654 (e.g. ARM or WD40). We predicted the interaction on the kinase domain for several interactors of the
655 BioID interactome as well as the one obtained in the presence of RAB29 over-expression, including the
656 known substrate RAB8A. The engagement in a substrate-like fashion with the catalytic core entails the
657 opening of the LRRK2 structure, with the detachment of the LRR and rearrangement of the entire N-
658 term domains. We previously showed that this conformation, that we similarly predicted for the
659 LRRK2:RAB10 complex, is compatible with distance restraints obtained by mass spectrometric mapping
660 of chemical crosslinking sites via XL-MS (Guaitoli et al., 2023). Moreover, if superimposed on the
661 active-like conformation of the most recent LRRK2 tetrameric structure, such predicted complexes fit
662 very well on the rest of the oligomer, with no clashes between the modelled LRRK2 chain and the rest
663 of the tetramer, further supporting the plausibility of such complexes (Guaitoli et al., 2023). We
664 speculate that partners engaging in this manner may represent putative substrates or function as
665 regulators of kinase domain activity. Strikingly, we rarely observed such interaction interface for
666 interactors enriched in presence of the MLi-2 inhibitor, which bind more frequently to the locked
667 conformation of LRRK2.

668 In conclusion, combining proximity proteomics with co-evolutionary and structural information helped
669 identifying distinct molecular networks linking LRRK2 to centrosomal biology and primary cilia. The

670 data may foster future functional analysis to further dissect these pathways to get a detailed picture
671 of the molecular pathophysiology underlying the cilia phenotypes caused by genetic variants in
672 different genes underlying familial forms of Parkinson's disease.

673

674 **Limitations of the study**

675 While the HEK293T system enables large-scale experimental throughput, it may not fully reflect the
676 neuronal context. Nonetheless, many neuronal proteins are known to be expressed in this cell line,
677 providing partial relevance. Another limitation is the low endogenous expression of LRRK2 in HEK293T
678 cells. As a result, the study relies on the overexpression of LRRK2 BioID fusion proteins, which may
679 introduce artifacts not present under physiological conditions.

680

681 **Data availability**

682 The mass spectrometry proteomics data have been deposited to the ProteomeXchange Consortium
683 via the PRIDE (Perez-Riverol et al., 2022) partner repository with the dataset identifier PXD048832 and
684 https://doi.org/10.6019/PXD048832 (BioID1, BioID2, miniTurbo), PXD048806 and
685 https://doi.org/10.6019/PXD048806 (LRRK2 proximity-proteomes MLi-2 vs. GZD-524) as well as
686 PXD048808 and https://doi.org/10.6019/PXD048808 (RAB29 co-expression). The data will be released
687 with the final publication of the peer-reviewed manuscript. The BioID interaction network and
688 associated co-evolutionary and structural analysis can accessed at the following URL:
689 (https://dip.bioinfolab.sns.it/explore/). The code used for the analysis is available at the following
690 links: https://github.com/raimondilab/distogram_analysis ,
691 https://github.com/raimondilab/Stable_complex_predictor. All data presented in the preprint version
692 of the manuscript, including MS RAW files, can be obtained upon request. A point-to-point protocol
693 for the BioID approach was deposited on Zenodo (DOI: 10.5281/zenodo.17045153).

694 **Author contributions**

695 M.E. and F.I. performed BioID experiments. M.E., F.I., P.M., F.R. and C.J.G. analyzed the primary BioID
696 data. P.M. and F.R. performed the post-analysis of primary BioID data. P.M., N.D.R. and F.R. wrote the
697 code for the bioinformatic workflow. C.J.G., F.R. and M.U. designed the study. M.E., F.I., P.M., F.R. and
698 C.J.G. wrote the manuscript.

699

700 **Acknowledgements**

701 We are grateful to the staff of the Core Facility for Medical Proteomics at the medical faculty of the
702 University of Tübingen for technical assistance. Furthermore, we gratefully acknowledge
703 computational resources of the Center for High Performance Computing (CHPC) at SNS. CJG received
704 funds from The Michael J. Fox Foundation for Parkinson's Research (grant ID: MJFF-8068.02, MJFF-
705 8068.04 and MJFF-023920) and iMed – the Helmholtz Initiative on Personalized Medicine.

706 **Literature**

707 Almawi, A.W., Matthews, L.A., and Guarne, A. (2017). FHA domains: Phosphopeptide binding and
708 beyond. *Prog Biophys Mol Biol 127*, 105-110 doi: 10.1016/j.pbiomolbio.2016.12.003.
709 Altenhoff, A.M., Train, C.M., Gilbert, K.J., Mediratta, I., Mendes de Farias, T., Moi, D., Nevers, Y.,
710 Radoykova, H.S., Rossier, V., Warwick Vesztrocy, A., Glover, N.M., and Dessimoz, C. (2021).
711 OMA orthology in 2021: website overhaul, conserved isoforms, ancestral gene order and
712 more. *Nucleic acids research 49*, D373-D379 doi: 10.1093/nar/gkaa1007.
713 Bang, Y., Kim, K.S., Seol, W., and Choi, H.J. (2016). LRRK2 interferes with aggresome formation for
714 autophagic clearance. *Mol Cell Neurosci 75*, 71-80 doi: 10.1016/j.mcn.2016.06.007.
715 Barenz, F., Inoue, D., Yokoyama, H., Tegha-Dunghu, J., Freiss, S., Draeger, S., Mayilo, D., Cado, I.,
716 Merker, S., Klinger, M., Hoeckendorf, B., Pilz, S., Hupfeld, K., Steinbeisser, H., Lorenz, H.,
717 Ruppert, T., Wittbrodt, J., and Gruss, O.J. (2013). The centriolar satellite protein SSX2IP
718 promotes centrosome maturation. *J Cell Biol 202*, 81-95 doi: 10.1083/jcb.201302122.
719 Beilina, A., Rudenko, I.N., Kaganovich, A., Civiero, L., Chau, H., Kalia, S.K., Kalia, L.V., Lobbestael, E.,
720 Chia, R., Ndukwe, K., Ding, J., Nalls, M.A., International Parkinson's Disease Genomics, C., North
721 American Brain Expression, C., Olszewski, M., Hauser, D.N., Kumaran, R., Lozano, A.M.,
722 Baekelandt, V., Greene, L.E., Taymans, J.M., Greggio, E., and Cookson, M.R. (2014). Unbiased
723 screen for interactors of leucine-rich repeat kinase 2 supports a common pathway for sporadic
724 and familial Parkinson disease. *Proceedings of the National Academy of Sciences of the United*
725 *States of America 111*, 2626-2631 doi: 10.1073/pnas.1318306111.
726 Bersuker, K., Peterson, C.W.H., To, M., Sahl, S.J., Savikhin, V., Grossman, E.A., Nomura, D.K., and
727 Olzmann, J.A. (2018). A Proximity Labeling Strategy Provides Insights into the Composition and
728 Dynamics of Lipid Droplet Proteomes. *Dev Cell 44*, 97-112 e117 doi:
729 10.1016/j.devcel.2017.11.020.
730 Boecker, C.A., and Holzbaur, E.L.F. (2021). Hyperactive LRRK2 kinase impairs the trafficking of axonal
731 autophagosomes. *Autophagy 17*, 2043-2045 doi: 10.1080/15548627.2021.1936933.
732 Boldt, K., van Reeuwijk, J., Lu, Q., Koutroumpas, K., Nguyen, T.M., Texier, Y., van Beersum, S.E., Horn,
733 N., Willer, J.R., Mans, D.A., Dougherty, G., Lamers, I.J., Coene, K.L., Arts, H.H., Betts, M.J., Beyer,
734 T., Bolat, E., Gloeckner, C.J., Haidari, K., Hetterschijt, L., Iaconis, D., Jenkins, D., Klose, F., Knapp,
735 B.*, et al.* (2016). An organelle-specific protein landscape identifies novel diseases and
736 molecular mechanisms. *Nature communications 7*, 11491 doi: 10.1038/ncomms11491.
737 Bonet-Ponce, L., Beilina, A., Williamson, C.D., Lindberg, E., Kluss, J.H., Saez-Atienzar, S., Landeck, N.,
738 Kumaran, R., Mamais, A., Bleck, C.K.E., Li, Y., and Cookson, M.R. (2020). LRRK2 mediates
739 tubulation and vesicle sorting from lysosomes. *Sci Adv 6* doi: 10.1126/sciadv.abb2454.
740 Branon, T.C., Bosch, J.A., Sanchez, A.D., Udeshi, N.D., Svinkina, T., Carr, S.A., Feldman, J.L., Perrimon,
741 N., and Ting, A.Y. (2018). Efficient proximity labeling in living cells and organisms with TurboID.
742 *Nat Biotechnol 36*, 880-887 doi: 10.1038/nbt.4201.
743 Carrion, M.D.P., Marsicano, S., Daniele, F., Marte, A., Pischedda, F., Di Cairano, E., Piovesana, E., von
744 Zweydorf, F., Kremmer, E., Gloeckner, C.J., Onofri, F., Perego, C., and Piccoli, G. (2017). The
745 LRRK2 G2385R variant is a partial loss-of-function mutation that affects synaptic vesicle
746 trafficking through altered protein interactions. *Sci Rep 7*, 5377 doi: 10.1038/s41598-017-
747 05760-9.
748 Chen, C., Xu, Z., Zhang, T., Lin, L., Lu, M., Xie, C., and Yu, X. (2019). Cep85 Relays Plk1 Activity to
749 Phosphorylated Nek2A for Its Timely Activation in Centrosome Disjunction. *iScience 11*, 114-
750 133 doi: 10.1016/j.isci.2018.12.013.
751 Cock, P.J., Antao, T., Chang, J.T., Chapman, B.A., Cox, C.J., Dalke, A., Friedberg, I., Hamelryck, T., Kauff,
752 F., Wilczynski, B., and de Hoon, M.J. (2009). Biopython: freely available Python tools for
753 computational molecular biology and bioinformatics. *Bioinformatics 25*, 1422-1423 doi:
754 10.1093/bioinformatics/btp163.
755 Cox, J., Hein, M.Y., Luber, C.A., Paron, I., Nagaraj, N., and Mann, M. (2014). Accurate proteome-wide
756 label-free quantification by delayed normalization and maximal peptide ratio extraction,

757 termed MaxLFQ. *Molecular & cellular proteomics : MCP 13*, 2513-2526 doi:
758 10.1074/mcp.M113.031591.
759 Dammermann, A., and Merdes, A. (2002). Assembly of centrosomal proteins and microtubule
760 organization depends on PCM-1. *J Cell Biol 159*, 255-266 doi: 10.1083/jcb.200204023.
761 Deniston, C.K., Salogiannis, J., Mathea, S., Snead, D.M., Lahiri, I., Matyszewski, M., Donosa, O.,
762 Watanabe, R., Bohning, J., Shiau, A.K., Knapp, S., Villa, E., Reck-Peterson, S.L., and Leschziner,
763 A.E. (2020). Structure of LRRK2 in Parkinson's disease and model for microtubule interaction.
764 *Nature 588*, 344-349 doi: 10.1038/s41586-020-2673-2.
765 Dhekne, H.S., Tonelli, F., Yeshaw, W.M., Chiang, C.Y., Limouse, C., Jaimon, E., Purlyte, E., Alessi, D.R.,
766 and Pfeffer, S.R. (2023). Genome-wide screen reveals Rab12 GTPase as a critical activator of
767 Parkinson's disease-linked LRRK2 kinase. *Elife 12* doi: 10.7554/eLife.87098.
768 Dhekne, H.S., Yanatori, I., Gomez, R.C., Tonelli, F., Diez, F., Schule, B., Steger, M., Alessi, D.R., and
769 Pfeffer, S.R. (2018). A pathway for Parkinson's Disease LRRK2 kinase to block primary cilia and
770 Sonic hedgehog signaling in the brain. *Elife 7* doi: 10.7554/eLife.40202.
771 Dobson-Stone, C., Hallupp, M., Shahheydari, H., Ragagnin, A.M.G., Chatterton, Z., Carew-Jones, F.,
772 Shepherd, C.E., Stefen, H., Paric, E., Fath, T., Thompson, E.M., Blumbergs, P., Short, C.L., Field,
773 C.D., Panegyres, P.K., Hecker, J., Nicholson, G., Shaw, A.D., Fullerton, J.M., Luty, A.A., Schofield,
774 P.R., Brooks, W.S., Rajan, N., Bennett, M.F*., et al.* (2020). CYLD is a causative gene for
775 frontotemporal dementia - amyotrophic lateral sclerosis. *Brain 143*, 783-799 doi:
776 10.1093/brain/awaa039.
777 Doncheva, N.T., Morris, J.H., Gorodkin, J., and Jensen, L.J. (2019). Cytoscape StringApp: Network
778 Analysis and Visualization of Proteomics Data. *Journal of proteome research 18*, 623-632 doi:
779 10.1021/acs.jproteome.8b00702.
780 Douanne, T., Andre-Gregoire, G., Thys, A., Trillet, K., Gavard, J., and Bidere, N. (2019). CYLD Regulates
781 Centriolar Satellites Proteostasis by Counteracting the E3 Ligase MIB1. *Cell Rep 27*, 1657-1665
782 e1654 doi: 10.1016/j.celrep.2019.04.036.
783 Eguether, T., Ermolaeva, M.A., Zhao, Y., Bonnet, M.C., Jain, A., Pasparakis, M., Courtois, G., and Tassin,
784 A.M. (2014). The deubiquitinating enzyme CYLD controls apical docking of basal bodies in
785 ciliated epithelial cells. *Nature communications 5*, 4585 doi: 10.1038/ncomms5585.
786 Ehebauer, M.T., and Arias, A.M. (2009). The structural and functional determinants of the Axin and
787 Dishevelled DIX domains. *BMC Struct Biol 9*, 70 doi: 10.1186/1472-6807-9-70.
788 Evans, R., O'Neill, M., Pritzel, A., Antropova, N., Senior, A., Green, T., Žídek, A., Bates, R., Blackwell, S.,
789 Yim, J., Ronneberger, O., Bodenstein, S., Zielinski, M., Bridgland, A., Potapenko, A., Cowie, A.,
790 Tunyasuvunakool, K., Jain, R., Clancy, E., Kohli, P., Jumper, J., and Hassabis, D. (2021). Protein
791 complex prediction with AlphaFold-Multimer. *bioRxiv* doi: 10.1101/2021.10.04.463034.
792 Fahn, S. (2003). Description of Parkinson's disease as a clinical syndrome. *Annals of the New York*
793 *Academy of Sciences 991*, 1-14 doi: 10.1111/j.1749-6632.2003.tb07458.x.
794 Filippini, F., Nola, S., Zahraoui, A., Roger, K., Esmaili, M., Sun, J., Wojnacki, J., Vlieghe, A., Bun, P.,
795 Blanchon, S., Rain, J.C., Taymans, J.M., Chartier-Harlin, M.C., Guerrera, C., and Galli, T. (2023).
796 Secretion of VGF relies on the interplay between LRRK2 and post-Golgi v-SNAREs. *Cell Rep 42*,
797 112221 doi: 10.1016/j.celrep.2023.112221.
798 Follett, J., and Farrer, M.J. (2021). LRRK2; a dynamic regulator of cellular trafficking. *Brain Res 1761*,
799 147394 doi: 10.1016/j.brainres.2021.147394.
800 Galaxy, C. (2024). The Galaxy platform for accessible, reproducible, and collaborative data analyses:
801 2024 update. *Nucleic acids research 52*, W83-W94 doi: 10.1093/nar/gkae410.
802 Gasser, T., Hardy, J., and Mizuno, Y. (2011). Milestones in PD genetics. *Mov Disord 26*, 1042-1048 doi:
803 10.1002/mds.23637.
804 Geisler, S., Holmstrom, K.M., Skujat, D., Fiesel, F.C., Rothfuss, O.C., Kahle, P.J., and Springer, W. (2010).
805 PINK1/Parkin-mediated mitophagy is dependent on VDAC1 and p62/SQSTM1. *Nat Cell Biol 12*,
806 119-131 doi: 10.1038/ncb2012.

807 Gloeckner, C.J., Boldt, K., Schumacher, A., Roepman, R., and Ueffing, M. (2007). A novel tandem affinity
808 purification strategy for the efficient isolation and characterisation of native protein
809 complexes. *Proteomics 7*, 4228-4234 doi: 10.1002/pmic.200700038.
810 Gloeckner, C.J., Boldt, K., and Ueffing, M. (2009). Strep/FLAG tandem affinity purification (SF-TAP) to
811 study protein interactions. *Current protocols in protein science / editorial board, John E Coligan*
812 *[et al] Chapter 19*, Unit19 20 doi: 10.1002/0471140864.ps1920s57.
813 Gloeckner, C.J., Boldt, K., von Zweydorf, F., Helm, S., Wiesent, L., Sarioglu, H., and Ueffing, M. (2010).
814 Phosphopeptide analysis reveals two discrete clusters of phosphorylation in the N-terminus
815 and the Roc domain of the Parkinson-disease associated protein kinase LRRK2. *Journal of*
816 *proteome research 9*, 1738-1745 doi: 10.1021/pr9008578.
817 Gloeckner, C.J., and Porras, P. (2020). Guilt-by-Association - Functional Insights Gained From Studying
818 the LRRK2 Interactome. *Front Neurosci 14*, 485 doi: 10.3389/fnins.2020.00485.
819 Grishin, N.V. (2001). KH domain: one motif, two folds. *Nucleic acids research 29*, 638-643 doi:
820 10.1093/nar/29.3.638.
821 Guaitoli, G., Raimondi, F., Gilsbach, B.K., Gomez-Llorente, Y., Deyaert, E., Renzi, F., Li, X., Schaffner, A.,
822 Jagtap, P.K., Boldt, K., von Zweydorf, F., Gotthardt, K., Lorimer, D.D., Yue, Z., Burgin, A., Janjic,
823 N., Sattler, M., Versees, W., Ueffing, M., Ubarretxena-Belandia, I., Kortholt, A., and Gloeckner,
824 C.J. (2016). Structural model of the dimeric Parkinson's protein LRRK2 reveals a compact
825 architecture involving distant interdomain contacts. *Proceedings of the National Academy of*
826 *Sciences of the United States of America 113*, E4357-4366 doi: 10.1073/pnas.1523708113.
827 Guaitoli, G., Zhang, X., Saitta, F., Miglionico, P., Silbermann, L.M., Ho, F.Y., von Zweydorf, F., Signorelli,
828 M., Tych, K., Fessas, D., Raimondi, F., Kortholt, A., and Gloeckner, C.J. (2023). Biophysical
829 analysis reveals autophosphorylation as an important regulator of LRRK2 dimerization. *bioRxiv*
830 doi: 10.1101/2023.08.11.549911.
831 Hall, E.A., Kumar, D., Prosser, S.L., Yeyati, P.L., Herranz-Perez, V., Garcia-Verdugo, J.M., Rose, L., McKie,
832 L., Dodd, D.O., Tennant, P.A., Megaw, R., Murphy, L.C., Ferreira, M.F., Grimes, G., Williams, L.,
833 Quidwai, T., Pelletier, L., Reiter, J.F., and Mill, P. (2023). Centriolar satellites expedite mother
834 centriole remodeling to promote ciliogenesis. *Elife 12* doi: 10.7554/eLife.79299.
835 Hallett, P.J., Engelender, S., and Isacson, O. (2019). Lipid and immune abnormalities causing age-
836 dependent neurodegeneration and Parkinson's disease. *J Neuroinflammation 16*, 153 doi:
837 10.1186/s12974-019-1532-2.
838 Hori, A., and Toda, T. (2017). Regulation of centriolar satellite integrity and its physiology. *Cellular and*
839 *molecular life sciences : CMLS 74*, 213-229 doi: 10.1007/s00018-016-2315-x.
840 Islam, M.S., Nolte, H., Jacob, W., Ziegler, A.B., Putz, S., Grosjean, Y., Szczepanowska, K., Trifunovic, A.,
841 Braun, T., Heumann, H., Heumann, R., Hovemann, B., Moore, D.J., and Kruger, M. (2016).
842 Human R1441C LRRK2 regulates the synaptic vesicle proteome and phosphoproteome in a
843 Drosophila model of Parkinson's disease. *Human molecular genetics 25*, 5365-5382 doi:
844 10.1093/hmg/ddw352.
845 Jennings, D., Huntwork-Rodriguez, S., Henry, A.G., Sasaki, J.C., Meisner, R., Diaz, D., Solanoy, H., Wang,
846 X., Negrou, E., Bondar, V.V., Ghosh, R., Maloney, M.T., Propson, N.E., Zhu, Y., Maciuca, R.D.,
847 Harris, L., Kay, A., LeWitt, P., King, T.A., Kern, D., Ellenbogen, A., Goodman, I., Siderowf, A.,
848 Aldred, J.*, et al.* (2022). Preclinical and clinical evaluation of the LRRK2 inhibitor DNL201 for
849 Parkinson's disease. *Science translational medicine 14*, eabj2658 doi:
850 10.1126/scitranslmed.abj2658.
851 Jian, F., Wang, S., Tian, R., Wang, Y., Li, C., Li, Y., Wang, S., Fang, C., Ma, C., and Rong, Y. (2024). The
852 STX17-SNAP47-VAMP7/VAMP8 complex is the default SNARE complex mediating
853 autophagosome-lysosome fusion. *Cell Res* doi: 10.1038/s41422-023-00916-x.
854 Kafka, A., Basic-Kinda, S., and Pecina-Slaus, N. (2014). The cellular story of dishevelleds. *Croat Med J*
855 *55*, 459-467 doi: 10.3325/cmj.2014.55.459.
856 Kaleb, K., Vesztrocy, A.W., Altenhoff, A., and Dessimoz, C. (2019). Expanding the Orthologous Matrix
857 (OMA) programmatic interfaces: REST API and the OmaDB packages for R and Python.
858 *F1000Res 8*, 42 doi: 10.12688/f1000research.17548.2.

859 Kalogeropulou, A.F., Purlyte, E., Tonelli, F., Lange, S.M., Wightman, M., Prescott, A.R., Padmanabhan,
860 S., Sammler, E., and Alessi, D.R. (2022). Impact of 100 LRRK2 variants linked to Parkinson's
861 Disease on kinase activity and microtubule binding. *The Biochemical journal* doi:
862 10.1042/BCJ20220161.
863 Kalogeropulou, A.F., Zhao, J., Bolliger, M.F., Memou, A., Narasimha, S., Molitor, T.P., Wilson, W.H.,
864 Rideout, H.J., and Nichols, R.J. (2018). P62/SQSTM1 is a novel leucine-rich repeat kinase 2
865 (LRRK2) substrate that enhances neuronal toxicity. *The Biochemical journal 475*, 1271-1293
866 doi: 10.1042/BCJ20170699.
867 Kanao, T., Venderova, K., Park, D.S., Unterman, T., Lu, B., and Imai, Y. (2010). Activation of FoxO by
868 LRRK2 induces expression of proapoptotic proteins and alters survival of postmitotic
869 dopaminergic neuron in Drosophila. *Human molecular genetics 19*, 3747-3758 doi:
870 10.1093/hmg/ddq289.
871 Khan, S.S., Jaimon, E., Lin, Y.E., Nikoloff, J., Tonelli, F., Alessi, D.R., and Pfeffer, S.R. (2024). Loss of
872 primary cilia and dopaminergic neuroprotection in pathogenic LRRK2-driven and idiopathic
873 Parkinson's disease. *Proceedings of the National Academy of Sciences of the United States of*
874 *America 121*, e2402206121 doi: 10.1073/pnas.2402206121.
875 Kiel, C., Vogt, A., Campagna, A., Chatr-aryamontri, A., Swiatek-de Lange, M., Beer, M., Bolz, S., Mack,
876 A.F., Kinkl, N., Cesareni, G., Serrano, L., and Ueffing, M. (2011). Structural and functional
877 protein network analyses predict novel signaling functions for rhodopsin. *Molecular systems*
878 *biology 7*, 551 doi: 10.1038/msb.2011.83.
879 Kim, D.I., Jensen, S.C., Noble, K.A., Kc, B., Roux, K.H., Motamedchaboki, K., and Roux, K.J. (2016). An
880 improved smaller biotin ligase for BioID proximity labeling. *Mol Biol Cell 27*, 1188-1196 doi:
881 10.1091/mbc.E15-12-0844.
882 Kluss, J.H., Bonet-Ponce, L., Lewis, P.A., and Cookson, M.R. (2022a). Directing LRRK2 to membranes of
883 the endolysosomal pathway triggers RAB phosphorylation and JIP4 recruitment. *Neurobiol Dis*
884 *170*, 105769 doi: 10.1016/j.nbd.2022.105769.
885 Kluss, J.H., Lewis, P.A., and Greggio, E. (2022b). Leucine-rich repeat kinase 2 (LRRK2): an update on the
886 potential therapeutic target for Parkinson's disease. *Expert Opin Ther Targets 26*, 537-546 doi:
887 10.1080/14728222.2022.2082937.
888 Kucera, M., Isserlin, R., Arkhangorodsky, A., and Bader, G.D. (2016). AutoAnnotate: A Cytoscape app
889 for summarizing networks with semantic annotations. *F1000Res 5*, 1717 doi:
890 10.12688/f1000research.9090.1.
891 Kumar, M., Acevedo-Cintron, J., Jhaldiyal, A., Wang, H., Andrabi, S.A., Eacker, S., Karuppagounder, S.S.,
892 Brahmachari, S., Chen, R., Kim, H., Ko, H.S., Dawson, V.L., and Dawson, T.M. (2020). Defects in
893 Mitochondrial Biogenesis Drive Mitochondrial Alterations in PARKIN-Deficient Human
894 Dopamine Neurons. *Stem Cell Reports 15*, 629-645 doi: 10.1016/j.stemcr.2020.07.013.
895 Lara Ordonez, A.J., Fasiczka, R., Fernandez, B., Naaldijk, Y., Fdez, E., Blanca Ramirez, M., Phan, S.,
896 Boassa, D., and Hilfiker, S. (2022). The LRRK2 signaling network converges on a centriolar
897 phospho-Rab10/RILPL1 complex to cause deficits in centrosome cohesion and cell
898 polarization. *Biol Open 11* doi: 10.1242/bio.059468.
899 Lara Ordonez, A.J., Fernandez, B., Fdez, E., Romo-Lozano, M., Madero-Perez, J., Lobbestael, E.,
900 Baekelandt, V., Aiastui, A., Lopez de Munain, A., Melrose, H.L., Civiero, L., and Hilfiker, S.
901 (2019). RAB8, RAB10 and RILPL1 contribute to both LRRK2 kinase-mediated centrosomal
902 cohesion and ciliogenesis deficits. *Human molecular genetics 28*, 3552-3568 doi:
903 10.1093/hmg/ddz201.
904 Li, B.J., Chen, H., Jiang, S.S., Wang, C.Y., Tuo, Q.H., Long, S.Y., Zhang, C.P., and Liao, D.F. (2020). PX
905 Domain-Containing Kinesin KIF16B and Microtubule-Dependent Intracellular Movements. *J*
906 *Membr Biol 253*, 101-108 doi: 10.1007/s00232-020-00110-9.
907 Li, P., Li, J., Wang, L., and Di, L.J. (2017). Proximity Labeling of Interacting Proteins: Application of BioID
908 as a Discovery Tool. *Proteomics 17* doi: 10.1002/pmic.201700002.
909 Li, X., Zhu, H., Huang, B.T., Li, X., Kim, H., Tan, H., Zhang, Y., Choi, I., Peng, J., Xu, P., Sun, J., and Yue, Z.
910 (2024). RAB12-LRRK2 complex suppresses primary ciliogenesis and regulates centrosome

homeostasis in astrocytes. *Nature communications 15*, 8434 doi: 10.1038/s41467-024-52723-6.

Lim, K.L., Chew, K.C., Tan, J.M., Wang, C., Chung, K.K., Zhang, Y., Tanaka, Y., Smith, W., Engelender, S., Ross, C.A., Dawson, V.L., and Dawson, T.M. (2005). Parkin mediates nonclassical, proteasomal-independent ubiquitination of synphilin-1: implications for Lewy body formation. *J Neurosci 25*, 2002-2009 doi: 10.1523/JNEUROSCI.4474-04.2005.

Liu, X., Salokas, K., Weldatsadik, R.G., Gawriyski, L., and Varjosalo, M. (2020). Combined proximity labeling and affinity purification-mass spectrometry workflow for mapping and visualizing protein interaction networks. *Nature protocols 15*, 3182-3211 doi: 10.1038/s41596-020-0365-x.

Lobbestael, E., Civiero, L., De Wit, T., Taymans, J.M., Greggio, E., and Baekelandt, V. (2016). Pharmacological LRRK2 kinase inhibition induces LRRK2 protein destabilization and proteasomal degradation. *Sci Rep 6*, 33897 doi: 10.1038/srep33897.

Manzoni, C., Denny, P., Lovering, R.C., and Lewis, P.A. (2015). Computational analysis of the LRRK2 interactome. *PeerJ 3*, e778 doi: 10.7717/peerj.778.

Matic, M., Miglionico, P., Tatsumi, M., Inoue, A., and Raimondi, F. (2023). GPCRome-wide analysis of G-protein-coupling diversity using a computational biology approach. *Nature communications 14*, 4361 doi: 10.1038/s41467-023-40045-y.

McGrath, E., Waschbusch, D., Baker, B.M., and Khan, A.R. (2021). LRRK2 binds to the Rab32 subfamily in a GTP-dependent manner via its armadillo domain. *Small GTPases 12*, 133-146 doi: 10.1080/21541248.2019.1666623.

Meixner, A., Boldt, K., Van Troys, M., Askenazi, M., Gloeckner, C.J., Bauer, M., Marto, J.A., Ampe, C., Kinkl, N., and Ueffing, M. (2011). A QUICK screen for Lrrk2 interaction partners--leucine-rich repeat kinase 2 is involved in actin cytoskeleton dynamics. *Molecular & cellular proteomics : MCP 10*, M110 001172 doi: 10.1074/mcp.M110.001172.

Meldal, B.H.M., Perfetto, L., Combe, C., Lubiana, T., Ferreira Cavalcante, J.V., Bye, A.J.H., Waagmeester, A., Del-Toro, N., Shrivastava, A., Barrera, E., Wong, E., Mlecnik, B., Bindea, G., Panneerselvam, K., Willighagen, E., Rappsilber, J., Porras, P., Hermjakob, H., and Orchard, S. (2022). Complex Portal 2022: new curation frontiers. *Nucleic acids research 50*, D578-D586 doi: 10.1093/nar/gkab991.

Mellacheruvu, D., Wright, Z., Couzens, A.L., Lambert, J.P., St-Denis, N.A., Li, T., Miteva, Y.V., Hauri, S., Sardiu, M.E., Low, T.Y., Halim, V.A., Bagshaw, R.D., Hubner, N.C., Al-Hakim, A., Bouchard, A., Faubert, D., Fermin, D., Dunham, W.H., Goudreault, M., Lin, Z.Y., Badillo, B.G., Pawson, T., Durocher, D., Coulombe, B.*, et al.* (2013). The CRAPome: a contaminant repository for affinity purification-mass spectrometry data. *Nature methods 10*, 730-736 doi: 10.1038/nmeth.2557.

Miglionico, P., Nemati Fard, L.A., Gloeckner, C.J., and Raimondi, F. (2024). Predicition and discovery of protein-protein direct interactions and stable complexes based on gene co-expression and co-evolution. *bioRxiv* doi: 10.1101/2024.10.05.616780.

Miller, G.K., Kuruvilla, S., Jacob, B., LaFranco-Scheuch, L., Bakthavatchalu, V., Flor, J., Flor, K., Ziegler, J., Reichard, C., Manfre, P., Firner, S., McNutt, T., Quay, D., Bellum, S., Doto, G., Ciaccio, P.J., Pearson, K., Valentine, J., Fuller, P., Fell, M., Tsuchiya, T., Williamson, T., and Wollenberg, G. (2023). Effects of LRRK2 Inhibitors in Nonhuman Primates. *Toxicol Pathol*, 1926233231205895 doi: 10.1177/01926233231205895.

Mohd Rafiq, N., Fujise, K., Rosenfeld, M.S., Xu, P., and De Camilli, P. (2024). Parkinsonism Sac domain mutation in Synaptojanin-1 affects ciliary properties in iPSC-derived dopaminergic neurons. *Proceedings of the National Academy of Sciences of the United States of America 121*, e2318943121 doi: 10.1073/pnas.2318943121.

Moreira, C., Kelemen, C.D., Obado, S.O., Zahedifard, F., Zhang, N., Holetz, F.B., Gauglitz, L., Dallagiovanna, B., Field, M.C., Kramer, S., and Zoltner, M. (2023). Impact of inherent biases built into proteomic techniques: Proximity labeling and affinity capture compared. *The Journal of biological chemistry 299*, 102726 doi: 10.1016/j.jbc.2022.102726.

Myasnikov, A., Zhu, H., Hixson, P., Xie, B., Yu, K., Pitre, A., Peng, J., and Sun, J. (2021). Structural analysis of the full-length human LRRK2. *Cell 184*, 3519-3527 e3510 doi: 10.1016/j.cell.2021.05.004.

Naaldijk, Y., Fernandez, B., Fasiczka, R., Fdez, E., Leghay, C., Croitoru, I., Kwok, J.B., Boulesnane, Y., Vizeneux, A., Mutez, E., Calvez, C., Destee, A., Taymans, J.M., Aragon, A.V., Yarza, A.B., Padmanabhan, S., Delgado, M., Alcalay, R.N., Chatterton, Z., Dzamko, N., Halliday, G., Ruiz-Martinez, J., Chartier-Harlin, M.C., and Hilfiker, S. (2024). A potential patient stratification biomarker for Parkinson s disease based on LRRK2 kinase-mediated centrosomal alterations in peripheral blood-derived cells. *NPJ Parkinsons Dis 10*, 12 doi: 10.1038/s41531-023-00624-8.

Orchard, S., Ammari, M., Aranda, B., Breuza, L., Briganti, L., Broackes-Carter, F., Campbell, N.H., Chavali, G., Chen, C., del-Toro, N., Duesbury, M., Dumousseau, M., Galeota, E., Hinz, U., Iannuccelli, M., Jagannathan, S., Jimenez, R., Khadake, J., Lagreid, A., Licata, L., Lovering, R.C., Meldal, B., Melidoni, A.N., Milagros, M.*, et al.* (2014). The MIntAct project--IntAct as a common curation platform for 11 molecular interaction databases. *Nucleic acids research 42*, D358-363 doi: 10.1093/nar/gkt1115.

Paisan-Ruiz, C., Jain, S., Evans, E.W., Gilks, W.P., Simon, J., van der Brug, M., Lopez de Munain, A., Aparicio, S., Gil, A.M., Khan, N., Johnson, J., Martinez, J.R., Nicholl, D., Marti Carrera, I., Pena, A.S., de Silva, R., Lees, A., Marti-Masso, J.F., Perez-Tur, J., Wood, N.W., and Singleton, A.B. (2004). Cloning of the gene containing mutations that cause PARK8-linked Parkinson's disease. *Neuron 44*, 595-600 doi: 10.1016/j.neuron.2004.10.023.

Park, S., Han, S., Choi, I., Kim, B., Park, S.P., Joe, E.H., and Suh, Y.H. (2016). Interplay between Leucine-Rich Repeat Kinase 2 (LRRK2) and p62/SQSTM-1 in Selective Autophagy. *PloS one 11*, e0163029 doi: 10.1371/journal.pone.0163029.

Pedregosa, F., Varoquaux, G., Gramfort, A., Michel, V., B., T., Griesel, O., Blondel, M., Prettenhofer, P., Weiss, R., Dubourg, V., Vanderplas, J., Passos, A., D., C., M., B., Perrot, M., and E., D. (2011). Scikit-learn: Machine Learning in Python. *Journal of Machine Learning Research 12*, 2825-2830 doi:

Perez-Riverol, Y., Bai, J., Bandla, C., Garcia-Seisdedos, D., Hewapathirana, S., Kamatchinathan, S., Kundu, D.J., Prakash, A., Frericks-Zipper, A., Eisenacher, M., Walzer, M., Wang, S., Brazma, A., and Vizcaino, J.A. (2022). The PRIDE database resources in 2022: a hub for mass spectrometry-based proteomics evidences. *Nucleic acids research 50*, D543-D552 doi: 10.1093/nar/gkab1038.

Piccoli, G., Condliffe, S.B., Bauer, M., Giesert, F., Boldt, K., De Astis, S., Meixner, A., Sarioglu, H., Vogt-Weisenhorn, D.M., Wurst, W., Gloeckner, C.J., Matteoli, M., Sala, C., and Ueffing, M. (2011). LRRK2 controls synaptic vesicle storage and mobilization within the recycling pool. *J Neurosci 31*, 2225-2237 doi: 10.1523/JNEUROSCI.3730-10.2011.

Piccoli, G., Onofri, F., Cirnaru, M.D., Kaiser, C.J., Jagtap, P., Kastenmuller, A., Pischedda, F., Marte, A., von Zweydorf, F., Vogt, A., Giesert, F., Pan, L., Antonucci, F., Kiel, C., Zhang, M., Weinkauf, S., Sattler, M., Sala, C., Matteoli, M., Ueffing, M., and Gloeckner, C.J. (2014). Leucine-rich repeat kinase 2 binds to neuronal vesicles through protein interactions mediated by its C-terminal WD40 domain. *Mol Cell Biol 34*, 2147-2161 doi: 10.1128/MCB.00914-13.

Pirooznia, S.K., Wang, H., Panicker, N., Kumar, M., Neifert, S., Dar, M.A., Lau, E., Kang, B.G., Redding-Ochoa, J., Troncoso, J.C., Dawson, V.L., and Dawson, T.M. (2022). Deubiquitinase CYLD acts as a negative regulator of dopamine neuron survival in Parkinson's disease. *Sci Adv 8*, eabh1824 doi: 10.1126/sciadv.abh1824.

Prosser, S.L., Tkach, J., Gheiratmand, L., Kim, J., Raught, B., Morrison, C.G., and Pelletier, L. (2022). Aggresome assembly at the centrosome is driven by CP110-CEP97-CEP290 and centriolar satellites. *Nat Cell Biol 24*, 483-496 doi: 10.1038/s41556-022-00869-0.

Purlyte, E., Dhekne, H.S., Sarhan, A.R., Gomez, R., Lis, P., Wightman, M., Martinez, T.N., Tonelli, F., Pfeffer, S.R., and Alessi, D.R. (2018). Rab29 activation of the Parkinson's disease-associated LRRK2 kinase. *The EMBO journal 37*, 1-18 doi: 10.15252/embj.201798099.

Qin, W., Cho, K.F., Cavanagh, P.E., and Ting, A.Y. (2021). Deciphering molecular interactions by proximity labeling. *Nature methods 18*, 133-143 doi: 10.1038/s41592-020-01010-5.

1014 Ragueneau, E., Shrivastava, A., Morris, J.H., Del-Toro, N., Hermjakob, H., and Porras, P. (2021). IntAct
1015 App: a Cytoscape application for molecular interaction network visualization and analysis.
1016 *Bioinformatics 37*, 3684-3685 doi: 10.1093/bioinformatics/btab319.
1017 Raig, N.D., Surridge, K.J., Sanz-Murillo, M., Dederer, V., Kramer, A., Schwalm, M.P., Elson, L., Chatterjee,
1018 D., Mathea, S., Hanke, T., Leschziner, A.E., Reck-Peterson, S.L., and Knapp, S. (2024). Type-II
1019 kinase inhibitors that target Parkinson's Disease-associated LRRK2. *bioRxiv*,
1020 2024.2009.2017.613365 doi: 10.1101/2024.09.17.613365.
1021 Rousseeuw, P.J. (1987). Silhouettes: A graphical aid to the interpretation and validation of cluster
1022 analysis. *Journal of Computational and Applied Mathematics 20*, 53-65 doi: 10.1016/0377-
1023 0427(87)90125-7.
1024 Roux, K.J., Kim, D.I., Raida, M., and Burke, B. (2012). A promiscuous biotin ligase fusion protein
1025 identifies proximal and interacting proteins in mammalian cells. *J Cell Biol 196*, 801-810 doi:
1026 10.1083/jcb.201112098.
1027 Sancho, R.M., Law, B.M., and Harvey, K. (2009). Mutations in the LRRK2 Roc-COR tandem domain link
1028 Parkinson's disease to Wnt signalling pathways. *Human molecular genetics 18*, 3955-3968 doi:
1029 10.1093/hmg/ddp337.
1030 Schmidt, S., Luecken, M.D., Trumbach, D., Hembach, S., Niedermeier, K.M., Wenck, N., Pflugler, K.,
1031 Stautner, C., Bottcher, A., Lickert, H., Ramirez-Suastegui, C., Ahmad, R., Ziller, M.J., Fitzgerald,
1032 J.C., Ruf, V., van de Berg, W.D.J., Jonker, A.J., Gasser, T., Winner, B., Winkler, J., Vogt
1033 Weisenhorn, D.M., Giesert, F., Theis, F.J., and Wurst, W. (2022). Primary cilia and SHH signaling
1034 impairments in human and mouse models of Parkinson's disease. *Nature communications 13*,
1035 4819 doi: 10.1038/s41467-022-32229-9.
1036 Shannon, P., Markiel, A., Ozier, O., Baliga, N.S., Wang, J.T., Ramage, D., Amin, N., Schwikowski, B., and
1037 Ideker, T. (2003). Cytoscape: a software environment for integrated models of biomolecular
1038 interaction networks. *Genome Res 13*, 2498-2504 doi: 10.1101/gr.1239303.
1039 Shin, W.H., Park, J.H., and Chung, K.C. (2020). The central regulator p62 between ubiquitin proteasome
1040 system and autophagy and its role in the mitophagy and Parkinson's disease. *BMB Rep 53*, 56-
1041 63 doi: 10.5483/BMBRep.2020.53.1.283.
1042 Simon-Sanchez, J., Schulte, C., Bras, J.M., Sharma, M., Gibbs, J.R., Berg, D., Paisan-Ruiz, C., Lichtner, P.,
1043 Scholz, S.W., Hernandez, D.G., Kruger, R., Federoff, M., Klein, C., Goate, A., Perlmutter, J.,
1044 Bonin, M., Nalls, M.A., Illig, T., Gieger, C., Houlden, H., Steffens, M., Okun, M.S., Racette, B.A.,
1045 Cookson, M.R*., et al.* (2009). Genome-wide association study reveals genetic risk underlying
1046 Parkinson's disease. *Nat Genet 41*, 1308-1312 doi: 10.1038/ng.487.
1047 Sowa, M.E., Bennett, E.J., Gygi, S.P., and Harper, J.W. (2009). Defining the human deubiquitinating
1048 enzyme interaction landscape. *Cell 138*, 389-403 doi: 10.1016/j.cell.2009.04.042.
1049 Steger, M., Diez, F., Dhekne, H.S., Lis, P., Nirujogi, R.S., Karayel, O., Tonelli, F., Martinez, T.N., Lorentzen,
1050 E., Pfeffer, S.R., Alessi, D.R., and Mann, M. (2017). Systematic proteomic analysis of LRRK2-
1051 mediated Rab GTPase phosphorylation establishes a connection to ciliogenesis. *Elife 6* doi:
1052 10.7554/eLife.31012.
1053 Stevens, D.A., Lee, Y., Kang, H.C., Lee, B.D., Lee, Y.I., Bower, A., Jiang, H., Kang, S.U., Andrabi, S.A.,
1054 Dawson, V.L., Shin, J.H., and Dawson, T.M. (2015). Parkin loss leads to PARIS-dependent
1055 declines in mitochondrial mass and respiration. *Proceedings of the National Academy of*
1056 *Sciences of the United States of America 112*, 11696-11701 doi: 10.1073/pnas.1500624112.
1057 Tasegian, A., Singh, F., Ganley, I.G., Reith, A.D., and Alessi, D.R. (2021). Impact of Type II LRRK2
1058 inhibitors on signaling and mitophagy. *The Biochemical journal 478*, 3555-3573 doi:
1059 10.1042/BCJ20210375.
1060 Taylor, S.S., Kaila-Sharma, P., Weng, J.H., Aoto, P., Schmidt, S.H., Knapp, S., Mathea, S., and Herberg,
1061 F.W. (2020). Kinase Domain Is a Dynamic Hub for Driving LRRK2 Allostery. *Frontiers in*
1062 *molecular neuroscience 13*, 538219 doi: 10.3389/fnmol.2020.538219.
1063 Teo, G., Liu, G., Zhang, J., Nesvizhskii, A.I., Gingras, A.C., and Choi, H. (2014). SAINTexpress:
1064 improvements and additional features in Significance Analysis of INTeractome software. *J*
1065 *Proteomics 100*, 37-43 doi: 10.1016/j.jprot.2013.10.023.

Tollenaere, M.A.X., Villumsen, B.H., Blasius, M., Nielsen, J.C., Wagner, S.A., Bartek, J., Beli, P., Mailand, N., and Bekker-Jensen, S. (2015). p38- and MK2-dependent signalling promotes stress-induced centriolar satellite remodelling via 14-3-3-dependent sequestration of CEP131/AZI1. *Nature communications 6*, 10075 doi: 10.1038/ncomms10075.

Treier, M., Staszewski, L.M., and Bohmann, D. (1994). Ubiquitin-dependent c-Jun degradation in vivo is mediated by the delta domain. *Cell 78*, 787-798 doi: 10.1016/s0092-8674(94)90502-9.

Tyanova, S., Temu, T., Sinitcyn, P., Carlson, A., Hein, M.Y., Geiger, T., Mann, M., and Cox, J. (2016). The Perseus computational platform for comprehensive analysis of (prote)omics data. *Nature methods 13*, 731-740 doi: 10.1038/nmeth.3901.

Vides, E.G., Adhikari, A., Chiang, C.Y., Lis, P., Purlyte, E., Limouse, C., Shumate, J.L., Spinola-Lasso, E., Dhekne, H.S., Alessi, D.R., and Pfeffer, S.R. (2022). A feed-forward pathway drives LRRK2 kinase membrane recruitment and activation. *Elife 11* doi: 10.7554/eLife.79771.

Waschbusch, D., Michels, H., Strassheim, S., Ossendorf, E., Kessler, D., Gloeckner, C.J., and Barnekow, A. (2014). LRRK2 transport is regulated by its novel interacting partner Rab32. *PloS one 9*, e111632 doi: 10.1371/journal.pone.0111632.

Wauters, L., Versees, W., and Kortholt, A. (2019). Roco Proteins: GTPases with a Baroque Structure and Mechanism. *Int J Mol Sci 20* doi: 10.3390/ijms20010147.

Wilhelm, L.P., Zapata-Munoz, J., Villarejo-Zori, B., Pellegrin, S., Freire, C.M., Toye, A.M., Boya, P., and Ganley, I.G. (2022). BNIP3L/NIX regulates both mitophagy and pexophagy. *The EMBO journal 41*, e111115 doi: 10.15252/embj.2022111115.

Xue, J., Zhang, J., Zhang, J., Liu, J., Wang, F., Li, K., and Liu, C. (2023). The Parkinson's disease-associated mutation LRRK2 G2385R alters mitochondrial biogenesis via the PGC-1alpha-TFAM pathway. *Mitochondrion 73*, 10-18 doi: 10.1016/j.mito.2023.09.002.

Yang, Y., Ran, J., Liu, M., Li, D., Li, Y., Shi, X., Meng, D., Pan, J., Ou, G., Aneja, R., Sun, S.C., and Zhou, J. (2014). CYLD mediates ciliogenesis in multiple organs by deubiquitinating Cep70 and inactivating HDAC6. *Cell Res 24*, 1342-1353 doi: 10.1038/cr.2014.136.

Yu, M., Arshad, M., Wang, W., Zhao, D., Xu, L., and Zhou, L. (2018). LRRK2 mediated Rab8a phosphorylation promotes lipid storage. *Lipids Health Dis 17*, 34 doi: 10.1186/s12944-018-0684-x.

Zhao, Y., Bracher-Smith, M., Li, Y., Harvey, K., Escott-Price, V., Lewis, P.A., and Manzoni, C. (2024). Transcriptomics and weighted protein network analyses of the LRRK2 protein interactome reveal distinct molecular signatures for sporadic and LRRK2 Parkinson's Disease. *NPJ Parkinsons Dis 10*, 144 doi: 10.1038/s41531-024-00761-8.

Zhao, Y., Vavouraki, N., Lovering, R.C., Escott-Price, V., Harvey, K., Lewis, P.A., and Manzoni, C. (2023). Tissue specific LRRK2 interactomes reveal a distinct striatal functional unit. *PLoS Comput Biol 19*, e1010847 doi: 10.1371/journal.pcbi.1010847.

Zheng, L., Bernard-Marissal, N., Moullan, N., D'Amico, D., Auwerx, J., Moore, D.J., Knott, G., Aebischer, P., and Schneider, B.L. (2017). Parkin functionally interacts with PGC-1α to preserve mitochondria and protect dopaminergic neurons. *Human molecular genetics 26*, 582-598 doi: 10.1093/hmg/ddw418.

Zhu, H., Hixson, P., Ma, W., and Sun, J. (2024). Pharmacology of LRRK2 with type I and II kinase inhibitors revealed by cryo-EM. *Cell Discov 10*, 10 doi: 10.1038/s41421-023-00639-8.

Zhu, H., Tonelli, F., Turk, M., Prescott, A., Alessi, D.R., and Sun, J. (2023). Rab29-dependent asymmetrical activation of leucine-rich repeat kinase 2. *Science 382*, 1404-1411 doi: 10.1126/science.adi9926.

Zimprich, A., Biskup, S., Leitner, P., Lichtner, P., Farrer, M., Lincoln, S., Kachergus, J., Hulihan, M., Uitti, R.J., Calne, D.B., Stoessl, A.J., Pfeiffer, R.F., Patenge, N., Carbajal, I.C., Vieregge, P., Asmus, F., Muller-Myhsok, B., Dickson, D.W., Meitinger, T., Strom, T.M., Wszolek, Z.K., and Gasser, T. (2004). Mutations in LRRK2 cause autosomal-dominant parkinsonism with pleomorphic pathology. *Neuron 44*, 601-607 doi: 10.1016/j.neuron.2004.11.005.

1117 **Tables:**

Accession	Gene name	Protein name	Jaccard score
Q5S007	LRRK2	Leucine-rich repeat serine/threonine-protein kinase 2 (bait)	1.000000
Q9NQC7	**CYLD**	**Ubiquitin carboxyl-terminal hydrolase CYLD**	**0.848485**
Q6P2H3	CEP85	Centrosomal protein of 85 kDa	0.846626
Q96JH7	VCPIP1	Deubiquitinating protein VCPIP1	0.834286
Q96L93	KIF16B	Kinesin-like protein KIF16B	0.832335
P78312	FAM193A	Protein FAM193A	0.817647
Q8NEY1	NAV1	Neuron navigator 1	0.817073
Q7Z2T5	TRMT1L	TRMT1-like protein	0.815951
Q5SZL2	CEP85L	Centrosomal protein of 85 kDa-like	0.810127
O95684	CEP43	Centrosomal protein 43	0.809816
Q96RS0	TGS1	Trimethylguanosine synthase	0.798742

1118

1119 **Table 1:** 10 IDs with the highest Jaccard score underlying identified “Cluster 2”. The DUB CYLD (bold)
1120 shows highest co-evolution to LRRK2.

1121

Accession	Protein name	Gene name	p-value	Log2 T-test difference
P81605	Dermcidin	DCD	2.91844	3.3
Q9UPN4	Centrosomal protein of 131 kDa	CEP131	4.15494	2.2
Q49A88	Coiled-coil domain-containing protein 14	CCDC14	5.39373	2.1
Q9Y2D8	Afadin- and alpha-actinin-binding protein	SSX2IP	2.98866	2.1
O75665	Oral-facial-digital syndrome 1 protein	OFD1	7.92350	2.0
Q15154	Pericentriolar material 1 protein	PCM1	6.62987	1.8
Q9UHB6	LIM domain and actin-binding protein 1	LIMA1	2.96451	1.7
Q8WXW3	Progesterone-induced-blocking factor 1	PIBF1	4.62801	1.5
Q6WCQ1	Myosin phosphatase Rho-interacting protein	MPRIP	7.40967	1.5
Q14596	Next to BRCA1 gene 1 protein	NBR1	3.34347	1.3
Q5TB80	Centrosomal protein of 162 kDa	CEP162	3.46643	1.3
Q8WWI1	LIM domain only protein 7	LMO7	5.84664	1.3

1122

1123 **Table 2:** Enriched proteins in the LRRK2 proximity proteome upon MLi-2 treatment (FDR-controlled T-
1124 test).

Accession	Protein name	Gene name	p-value (-log10)	Log2 T-test difference
O14966	Ras-related protein Rab-7L1	RAB29	9,72545	10,5
Q8IZA0	Dyslexia-associated protein KIAA0319-like protein	KIAA0319L	5,00209	4,9
Q6WKZ4	Rab11 family-interacting protein 1	RAB11FIP1	4,56815	4,6
O15126	Secretory carrier-associated membrane protein 1	SCAMP1	4,09385	3,5
Q9UIQ6	Leucyl-cystinyl aminopeptidase;Leucyl-cystinyl aminopeptidase, pregnancy serum form	LNPEP	4,33552	3,4
Q9H2J7	Sodium-dependent neutral amino acid transporter B(0)AT2	SLC6A15	5,06972	2,9
Q96QD8	Sodium-coupled neutral amino acid transporter 2	SLC38A2	2,89271	2,9
Q13586	Stromal interaction molecule 1	STIM1	3,12115	2,8
P98194	Calcium-transporting ATPase type 2C member 1	ATP2C1	5,00347	2,6
Q9H2H9	Sodium-coupled neutral amino acid transporter 1	SLC38A1	2,37723	2,6
O75976	Carboxypeptidase D	CPD	3,20952	2,6
Q14126	Desmoglein-2	DSG2	4,31421	2,5
P51809	Vesicle-associated membrane protein 7	VAMP7	4,02209	2,5
Q8NDI1	EH domain-binding protein 1	EHBP1	2,37346	2,5
Q8TBA6	Golgin subfamily A member 5	GOLGA5	3,0259	2,4
Q9BXF6	Rab11 family-interacting protein 5	RAB11FIP5	2,9101	2,4
Q7L804	Rab11 family-interacting protein 2	RAB11FIP2	3,33154	2,2
Q6IAA8	Ragulator complex protein LAMTOR1	LAMTOR1	3,23604	2,1
P61006	Ras-related protein Rab-8A	RAB8A	3,56486	2,1
P11717	Cation-independent mannose-6-phosphate receptor	IGF2R	5,71543	2,0
Q13190	Syntaxin-5	STX5	3,88884	2,0
Q15836;P63027	Vesicle-associated membrane protein 3;Vesicle-associated membrane protein 2	VAMP3;VAMP2	3,67019	2,0
Q92692	Nectin-2	PVRL2	3,06334	2,0
Q6NXT4	Zinc transporter 6	SLC30A6	3,47208	1,8
Q96A65	Exocyst complex component 4	EXOC4	2,51947	1,7
Q14141	Septin-6	Sept6	3,87782	1,7
Q04656	Copper-transporting ATPase 1	ATP7A	2,77415	1,7
Q7Z2W4	Zinc finger CCCH-type antiviral protein 1	ZC3HAV1	2,62567	1,6
P78310	Coxsackievirus and adenovirus receptor	CXADR	2,87956	1,4
P08195	4F2 cell-surface antigen heavy chain	SLC3A2	2,43497	1,4
P02786	Transferrin receptor protein 1;Transferrin receptor protein 1, serum form	TFRC	3,21618	1,3
Q07960	Rho GTPase-activating protein 1	ARHGAP1	2,65929	1,3
O60271	C-Jun-amino-terminal kinase-interacting protein 4	SPAG9	3,80826	1,3
P42167	Lamina-associated polypeptide 2, isoforms beta/gamma;Thymopoietin;Thymopentin	TMPO	3,54449	1,2
Q9BSJ8	Extended synaptotagmin-1	ESYT1	3,59064	1,0
Q14739	Lamin-B receptor	LBR	3,12029	0,8

Table 3: Enriched proteins in the RAB29-depended LRRK2 proximity proteome (FDR-controlled T-test).

1128 **Figures**

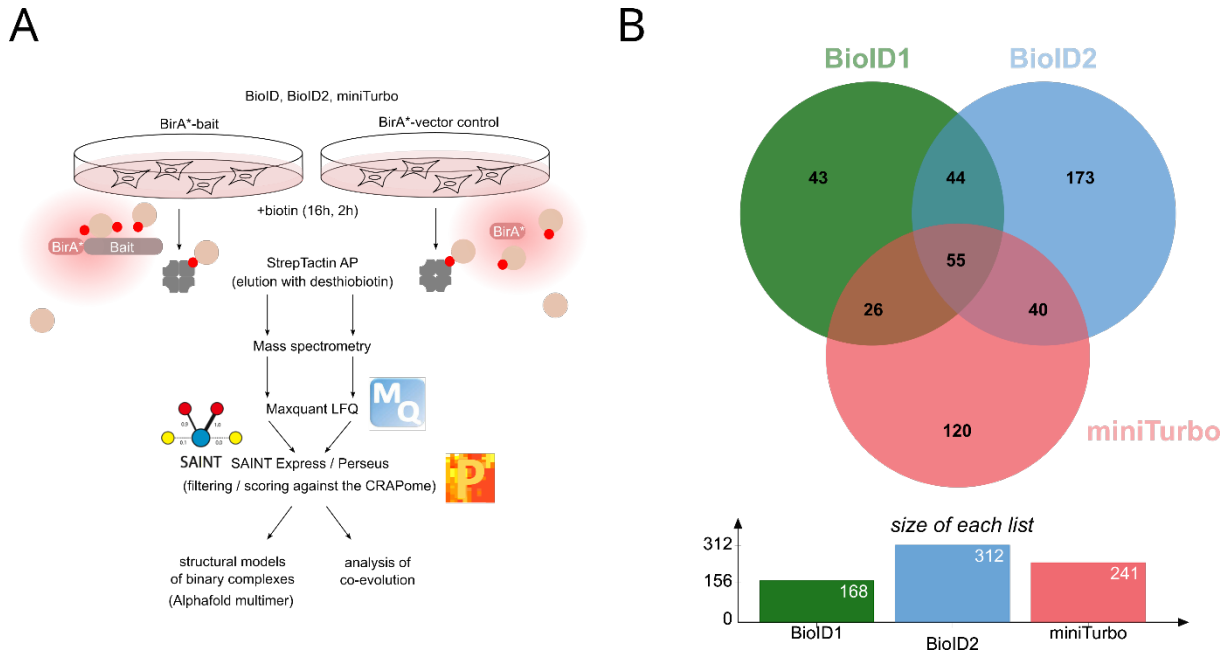

1129

1130 **Figure 1:** (A) Workflow of the BioID analysis and post processing of the data. (B) Overlap between the
1131 different BioID approaches. Enriched proteins were determined by relative label-free quantification
1132 (combined with an FDR-controlled T-test, p=0.05) of BioID LRRK2 vs the corresponding tag-only
1133 control: BioID1-LRRK2/BioID1-tag: N=8, BioID2-LRRK2/BioID2: N=9, miniTurbo-LRRK2/miniTurbo tag:
1134 N=8.

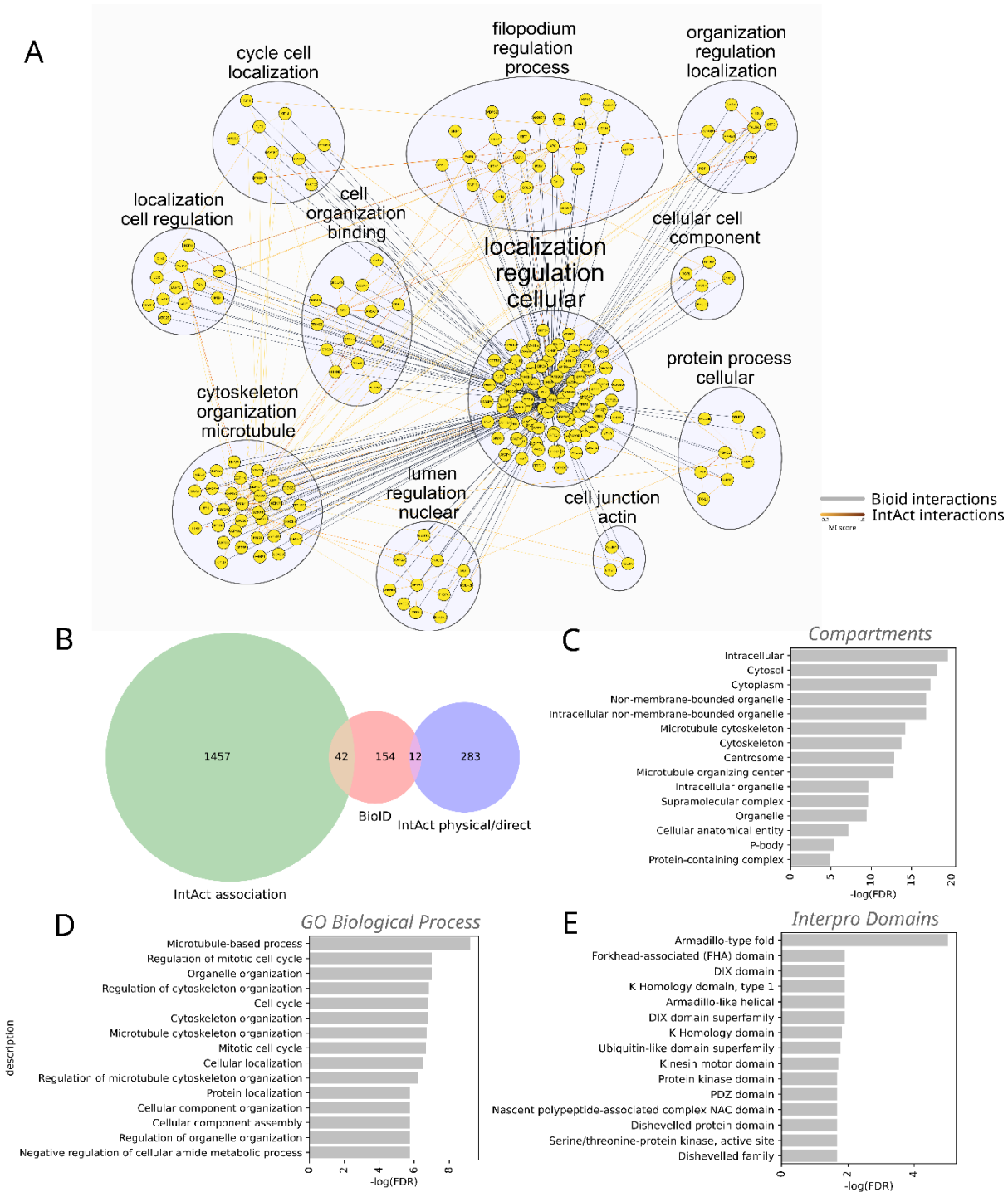

Figure 2: LRRK2 interactome functional enrichment. A) the LRRK2 BioID interaction network was mapped on known PPIs from IntAct via Cytoscape. The edges' color and thickness for mapped interactions are proportional to IntAct MI score, else they are colored in gray with constant thickness. Modules within the network have been identified through the Glay method of the Autoannotate app and nodes colored accordingly. Labels were calculated using the 'Adjacent Words' setting of the WordCloud algorithm, based on significantly enriched (FDR < 0.01) Gene Ontology (GO) Biological Processes and Cellular Component terms associated with each gene in the network ; B) Venn diagram showing the overlap between the BioID interaction sets and known LRRK2 interactions in IntAct;

1144 barplots showing the top 15 most significant terms obtained through String's functional enrichment of
1145 C) Compartments, D) GO Biological Process and D) Interpro domains.

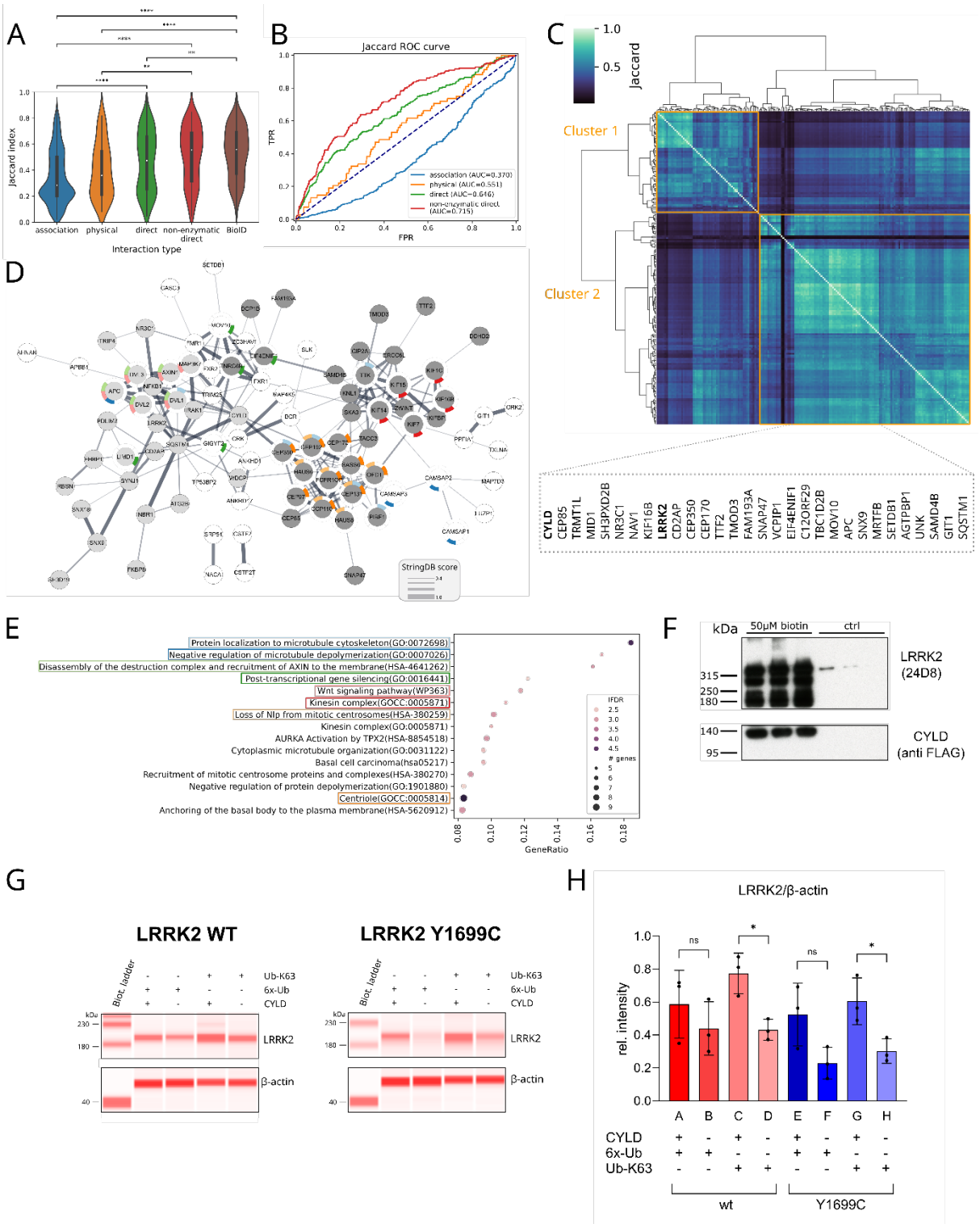

Figure 3: Co-evolution analysis of LRRK2 interactome. (A) Distribution of co-evolution metric (i.e. Jaccard score) among the different LRRK2 interaction sets, including IntAct interaction types and BIOID. P-values have been computed with the Wilcoxon rank-sum, two-sided test with Bonferroni correction (* $P < 0.05$, ** $P < 0.001$, *** $P < 0.001$, **** $P < 0.0001$). Violin plots show the median as the white central dot and first and third quartiles as bounds of the thicker black line (box); the whiskers extend to the last data point within 1.5 times the interquartile range (IQR)

1153 from the box's boundaries. (B) predictiveness of LRRK2 interaction type via co-evolution (C)
1154 Heatmap showing the hierarchical clustering based on the degree of co-evolution (Jaccard score) of
1155 the LRRK2 proximity proteome. (D) String network of the proteins most co-evolved with LRRK2
1156 participating to cluster 2. Nodes are colored in gray or light-gray according to modules membership
1157 determined with the MCL approach available from the Cytoscape clusterMaker app. Node rims are
1158 colored according to enriched processes. (E) Dot plot showing top 15 significantly enriched (FDR < 0.01)
1159 categories from the string network of cluster 2. Values on the x axis display the ratio of genes of the
1160 term participating to the network over the total number of genes in that category. The ratio of the dot
1161 is proportional to the number of genes of that category in the network, while the node color is the
1162 darker the more significant is the category enrichment. Only categories with at least 5 genes have been
1163 displayed. Representative, enriched categories have been colored with the same color scheme as in
1164 panel (D). (F) Validation of CYLD as part of the LRRK2 proximity proteome. Due to the lack of suitable
1165 antibodies for detecting endogenous CYLD, a FLAG-HA–tagged CYLD construct was recombinantly
1166 expressed for this experiment, in contrast to the mass spectrometry–based approach, which relied on
1167 endogenous protein levels. (G, H) CYLD co-expression enhances LRRK2 protein stability in HEK293T
1168 cells. HEK293T cells were transfected with either LRRK2 wild-type (WT) or the Y1699C variant, along
1169 with HA-tagged ubiquitin constructs: wild-type ubiquitin (WT-Ub) or a K63-only ubiquitin mutant (Ub-
1170 K63), which permits conjugation exclusively at lysine 63. CYLD or an empty vector control (pcDNA3.0)
1171 was co-expressed in each condition. Protein levels were assessed by capillary-based Western blotting
1172 with fluorescence detection. (G) Reconstructed Western blot signals. (H) Quantification of LRRK2
1173 protein levels from three technical replicates (same biological samples analyzed in three independent
1174 capillary Western runs). Statistical significance was assessed using unpaired two-tailed t-tests.

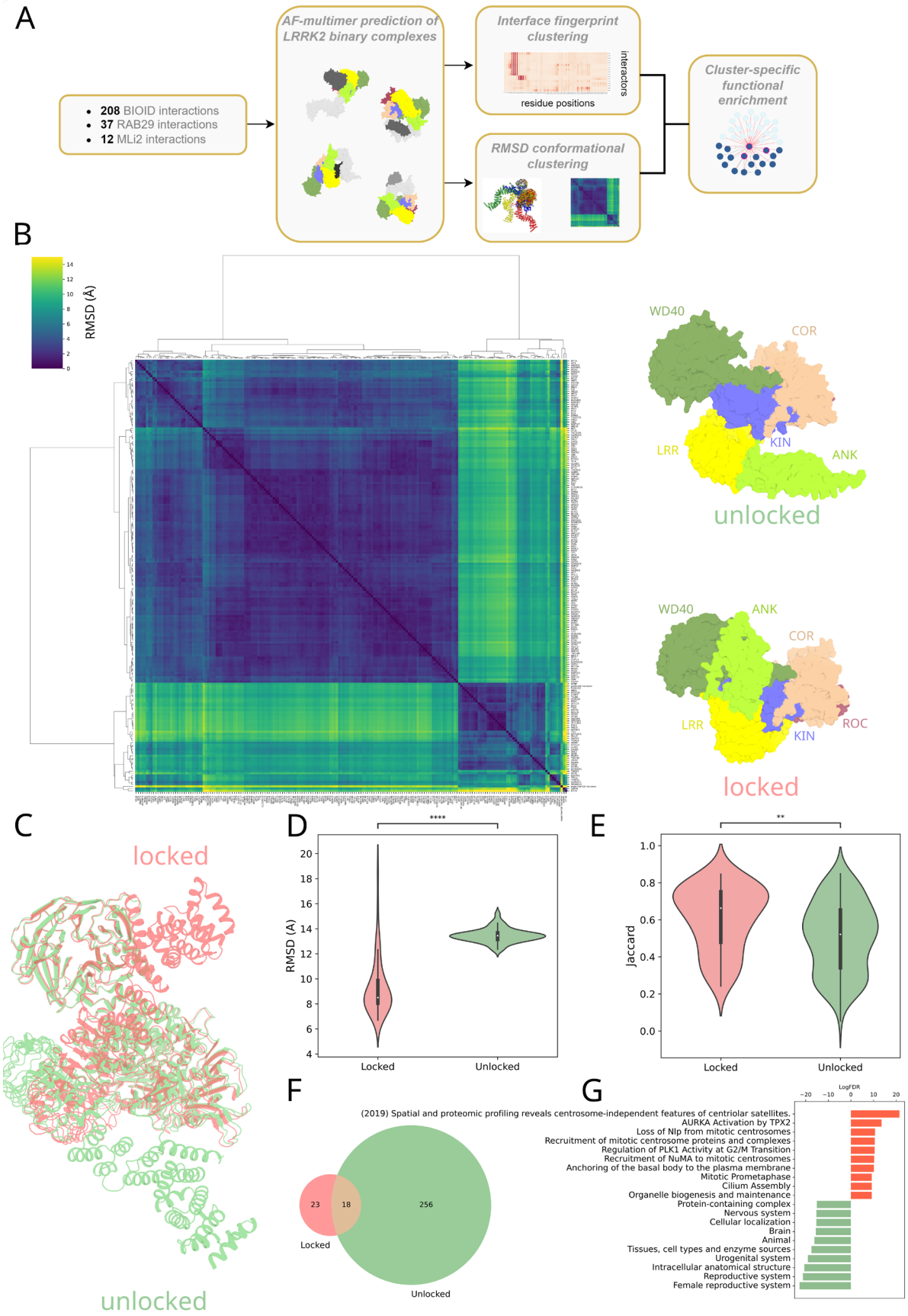

Figure 4: 3D complexes prediction and analysis of LRRK2 interactome (A) workflow of the structural bioinformatics analysis of LRRK2 interactome; (B) on the left the heatmap showing the hierarchical

1178 clustering based on pairwise RMSD calculation of LRRK2's chain in the different complexes. On the
1179 right two representative conformations of LRRK2 in the "locked" and "unlocked" conformation to mark
1180 the two main clusters; (C) cartoon representation of "locked" (tomato) and "unlocked" (light green)
1181 superimposed LRRK2 conformations; (D) violin plot of the distribution of RMSD calculated with respect
1182 to the reference LRRK2 experimental structure (PDB 7LHW) for the locked and unlocked clusters. Color
1183 scheme as in (C); (E) distribution of the Jaccard score for the locked and unlocked clusters. Color
1184 scheme as in (C). P-values for violin plots in D and E have been computed with the Wilcoxon
1185 rank-sum, two-sided test (* $P < 0.05$, ** $P < 0.001$, *** $P < 0.001$, **** $P < 0.0001$). Violin plots
1186 show the median as the white central dot and first and third quartiles as bounds of the thicker
1187 black line (box); the whiskers extend to the last data point within 1.5 times the interquartile
1188 range (IQR) from the box's boundaries; (F) Venn diagram of the enriched terms in the locked and
1189 unlocked clusters. Color scheme as in (C); (E) Top 10 exclusively enriched (FDR<0.01) terms in the
1190 locked and unlocked clusters.

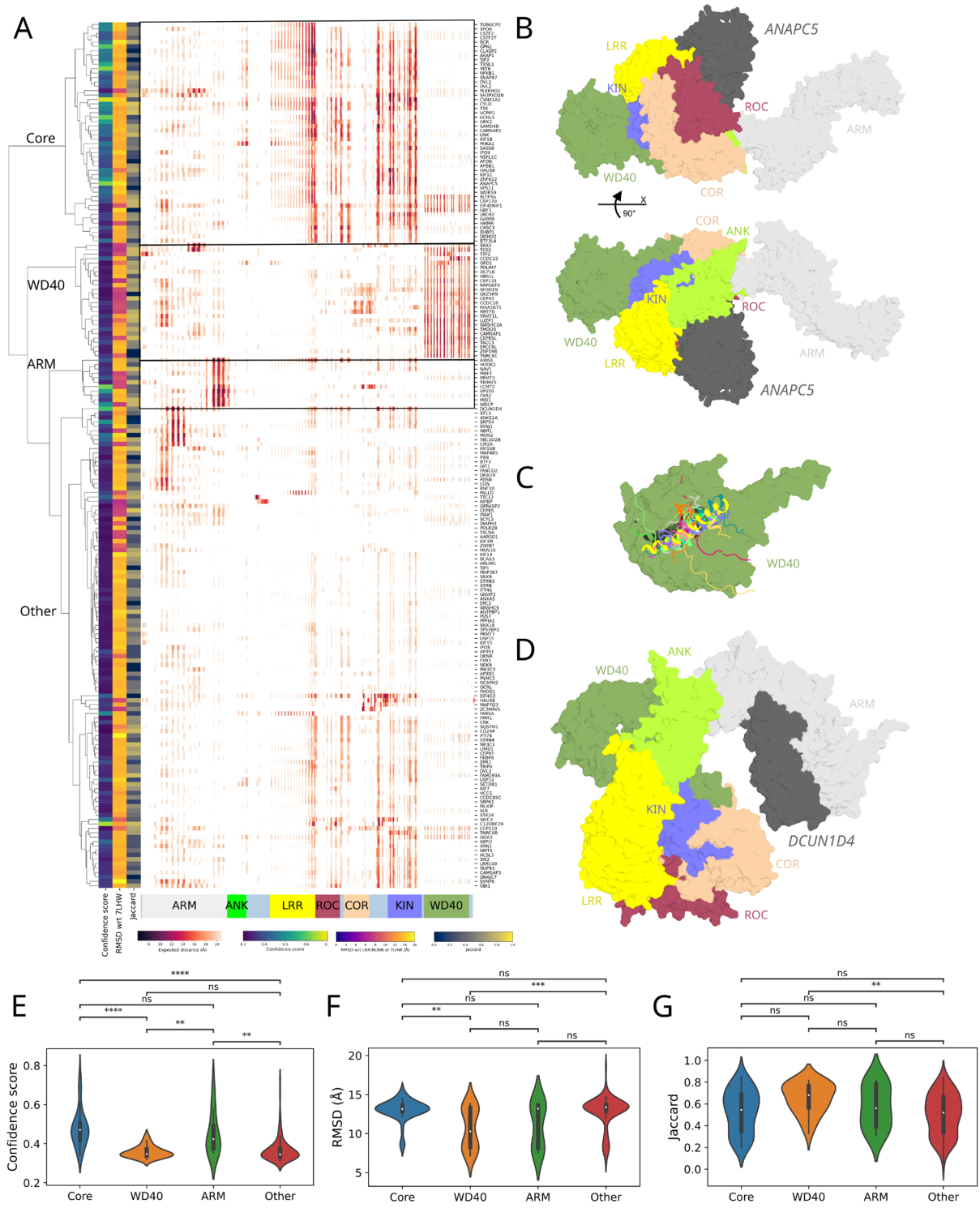

Figure 5: Interface analysis of LRRK2's 3D interactome (A) interface fingerprint of the LRRK2 complexes via distogram calculation. Cells contain the minimum expected distance obtained from the distograms of any residue of each interactor (row) to every residue in LRRK2 (column). Rows are color annotated based on confidence score, Jaccard and RMSD from reference LRRK2 structure (PDB: 7LHW); (B) representative structure of the Core cluster (i.e. LRRK2-ANAPC5 complex); (C) representative structures of the WD40 cluster; (D) representative structures of the ARM binding mode cluster (i.e. LRRK2- DCUN1D4 complex); distribution among different interface cluster of the (E) confidence score,

(F) RMSD and (G) Jaccard score descriptors. P-values have been computed with the Wilcoxon rank-sum, two-sided test with Bonferroni correction (* $P < 0.05$, ** $P < 0.001$, *** $P < 0.001$, **** $P < 0.0001$). Violin plots show the median as the white central dot and first and third quartiles as bounds of the thicker black line (box); the whiskers extend to the last data point within 1.5 times the interquartile range (IQR) from the box's boundaries.

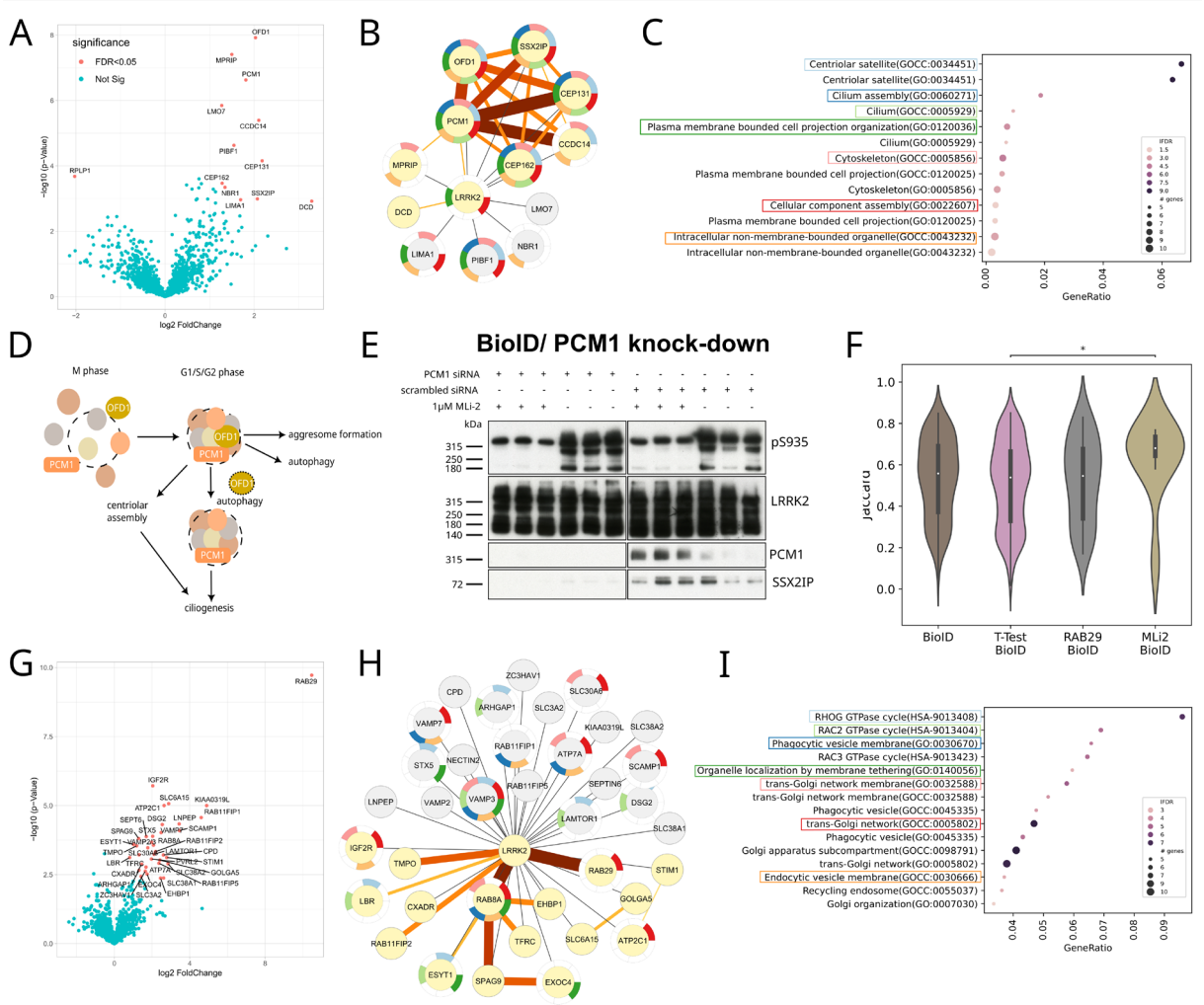

Figure 6: Different effects of type I and type II inhibitors and RAB29 on the LRRK2 proximity proteome. (A) MLi-2 vs DMSO. (B) Stringified network of the MLi-2 interactome from (A) mapped to IntAct known interactions. Edges' color and thickness for mapped interactions are proportional to IntAct MI score, else they are colored in gray with constant thickness. Node rims are colored according to enriched processes; (C) Dot plot showing top 15 significantly enriched (FDR < 0.01) categories from the LRRK2-MLi-2 interactome. Values on the x axis display the ratio of genes of the term participating to the network over the total number of genes in that category. The ratio of the dot is proportional to the number of genes of that category in the network, while the node color is the darker the more significant is the category enrichment. Only categories with at least 5 genes have been displayed. Representative, enriched categories have been colored with the same color scheme as in panel C. (D) Scheme highlighting the function of centriolar satellites and the core protein PCM1 in ciliation ((Hori and Toda, 2017), modified) (E) BioID analysis following PCM1 knockdown and MLi-2 treatment. Shown are eluates obtained after streptavidin-based enrichment of biotinylated proteins. (F) Violin plot reporting the Jaccard Score distribution in different data sets. P-values have been computed with the Wilcoxon rank-sum, two-sided test with Bonferroni correction (* $P < 0.05$). Violin plots

1220 show the median as the white central dot and first and third quartiles as bounds of the thicker
1221 black line (box); the whiskers extend to the last data point within 1.5 times the interquartile
1222 range (IQR) from the box's boundaries; (G) mt-LRRK2 proximity proteome in dependence of RAB29
1223 co-expression: RAB29 redirects LRRK2 to lysosomal PPI networks; (H) Stringified network of the RAB29
1224 over-expression interactome from (G) mapped to IntAct known interactions. Edges' color and thickness
1225 for mapped interactions are proportional to IntAct MI score, else they are colored in gray with constant
1226 thickness. Node rims are colored according to enriched processes; (I) Dot plot showing top 15
1227 significantly enriched (FDR < 0.01) categories from the LRRK2-RAB29 over-expression interactome.
1228 Values on the x axis display the ratio of genes of the term participating to the network over the total
1229 number of genes in that category. The ratio of the dot is proportional to the number of genes of that
1230 category in the network, while the node color is the darker the more significant is the category
1231 enrichment. Only categories with at least 5 genes have been displayed. Representative, enriched
1232 categories have been colored with the same color scheme as in panel H.

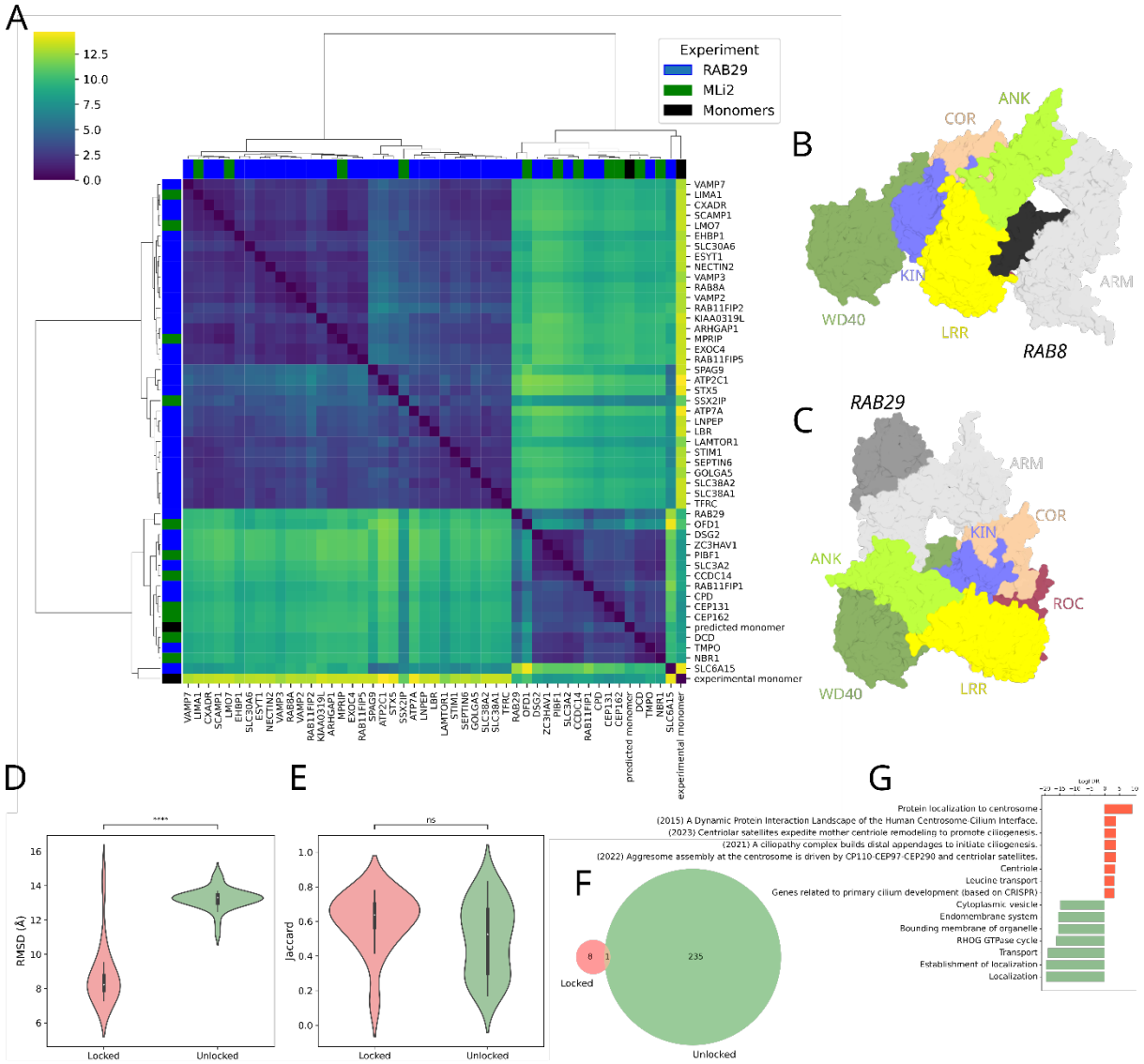

Figure 7: AF-structural modeling of MLi-2 and Rab29 interactomes. (A) Hierarchical clustering of pairwise RMSD of LRRK2 chain in the different complexes; B) LRRK2-RAB8A predicted complex; (C) LRRK2-RAB29 predicted complex; (D) violin plot of the distribution of RMSD calculated with respect to the reference LRRK2 experimental structure (PDB 7LHW) for the locked and unlocked clusters. Color scheme as in 4C; (E) distribution of the Jaccard score for the locked and unlocked clusters. Color scheme as in 4C. P-values in violin plots in (D) and (E) have been computed with the Wilcoxon rank-sum, two-sided test (* $P < 0.05$, ** $P < 0.001$, *** $P < 0.001$, **** $P < 0.0001$). Violin plots show the median as the white central dot and first and third quartiles as bounds of the thicker black line (box); the whiskers extend to the last data point within 1.5 times the interquartile range (IQR) from the box's boundaries; (F) Venn diagram of the enriched terms in the locked and unlocked clusters. Color scheme as in 4C; (G) Top exclusively enriched (FDR<0.01) terms in the locked and unlocked clusters. Color scheme as in 4C.

1246 **Supplemental Information**

1247 **Supplemental Tables**

1248 **Table S1:** LRRK2 proximity proteomes obtained with BioID1, BioID2 and miniTurbo as well as the
1249 Rab29-dependent LRRK2-mT and the inhibitor-dependent LRRK2-mT proximity proteomes.

1250 **Table S2:** (A) Co-evolutionary and structural features of BioID interactors. (B) Over-representation
1251 analysis of protein clusters defined via co-evolution. (C) Over-representation analysis of protein
1252 clusters defined via RMSD clustering of AF-multimer predicted complexes. (D) Over-representation
1253 analysis of protein clusters defined via Interaction fingerprint clustering of AF-multimer predicted
1254 complexes. (E) Over-representation analysis of protein clusters defined via RMSD clustering of AF-
1255 multimer predicted complexes of the RAB29-overexpression and MLi-2 interactomes.

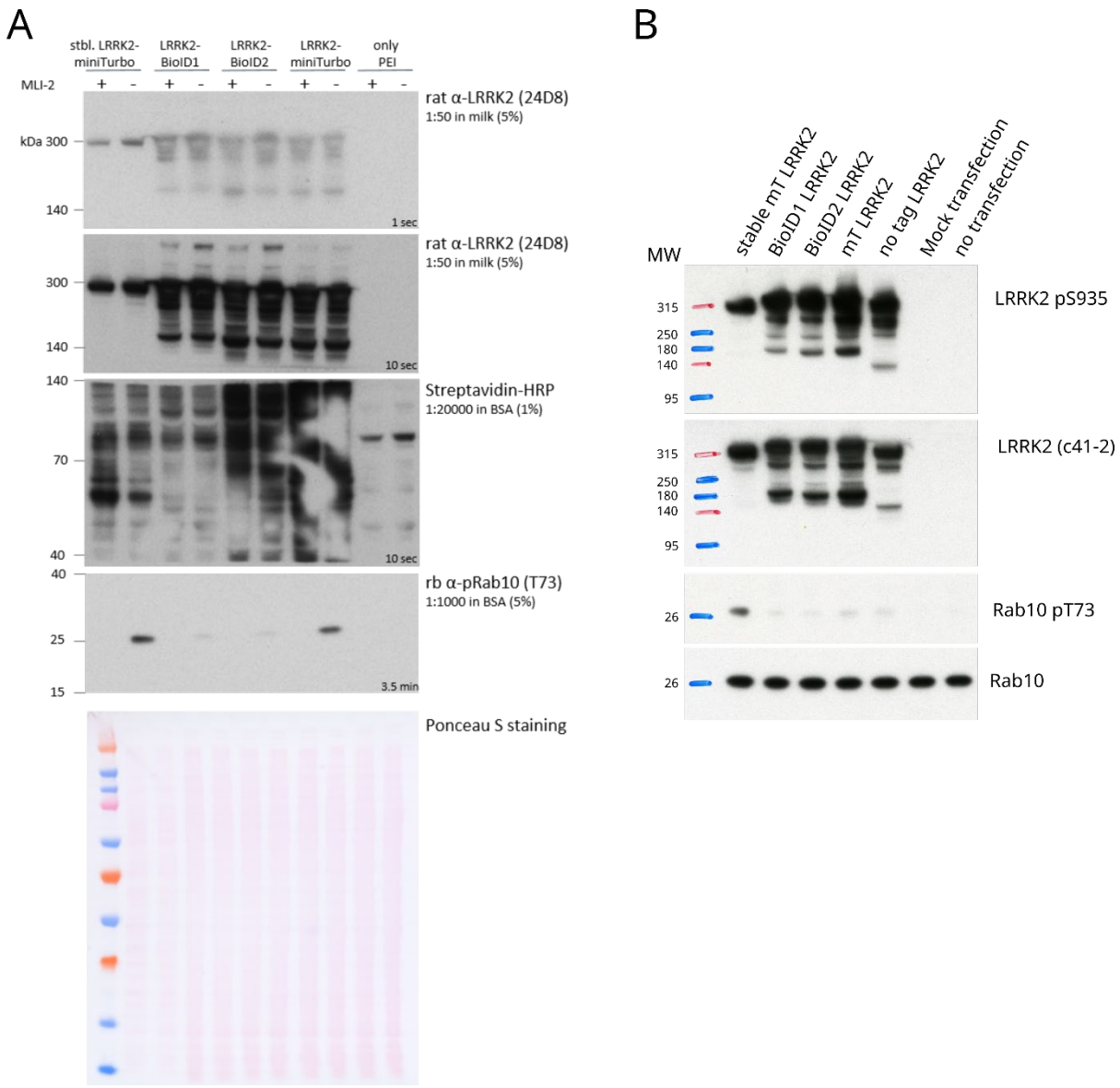

Supplemental Figure 1: Western blot, pRab10, pS935 and biotinylation – comparison BioID1, BioID2, miniTurbo. To ensure functional BioID-fusion proteins, LRRK2 phosphorylation at S935 and Rab10 phosphorylation was assessed. (A) The different BioID LRRK2 constructs show sufficient biotinylation of proteins as well as MLi-2-responsive Rab10 phosphorylation. (B) All constructs are phosphorylated at S935 (top panel). Replication of LRRK2-mediated Rab10 phosphorylation (last panel) demonstrating functional BioID fusion proteins.

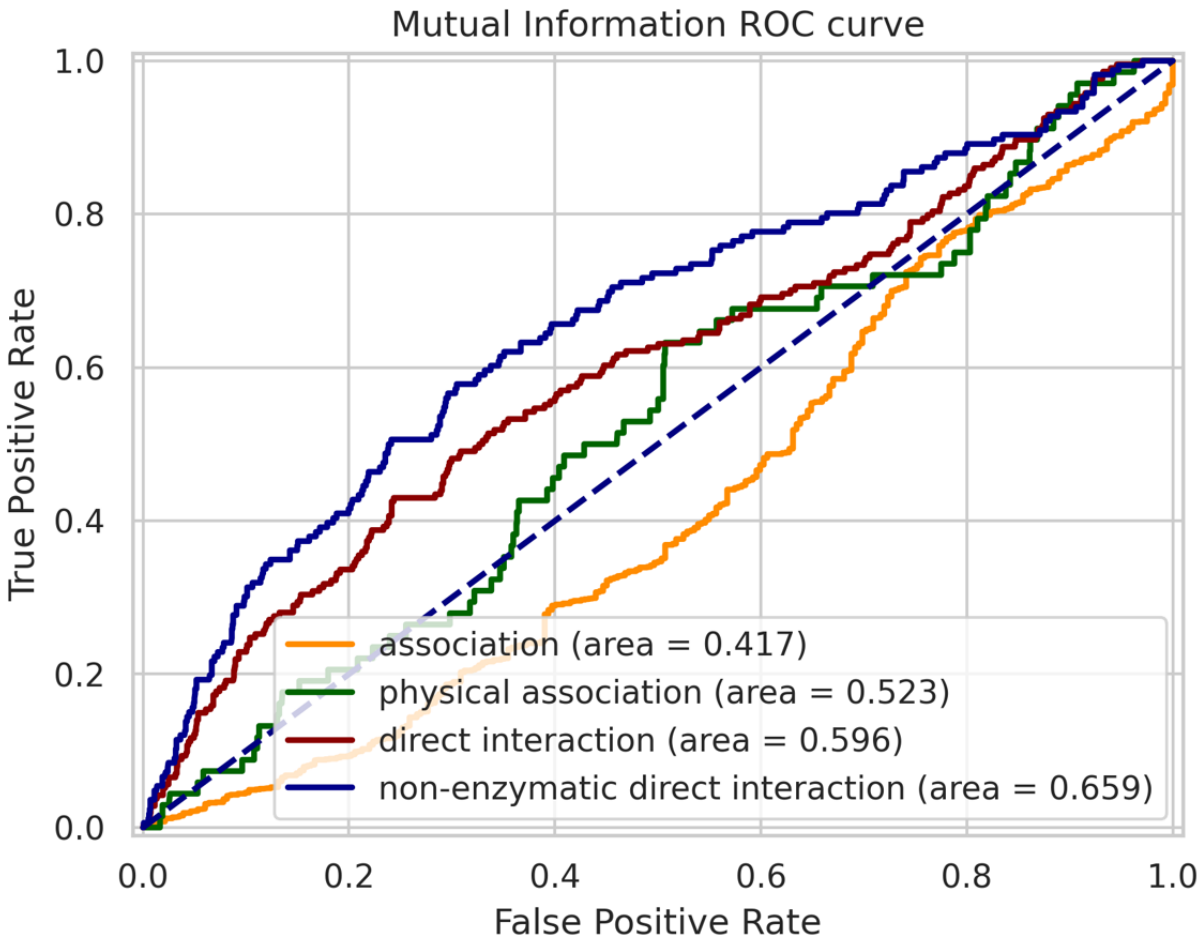

Supplemental Figure 2: ROC Curve of prediction with Mutual Information (MI) of LRRK2's IntAct interaction types.

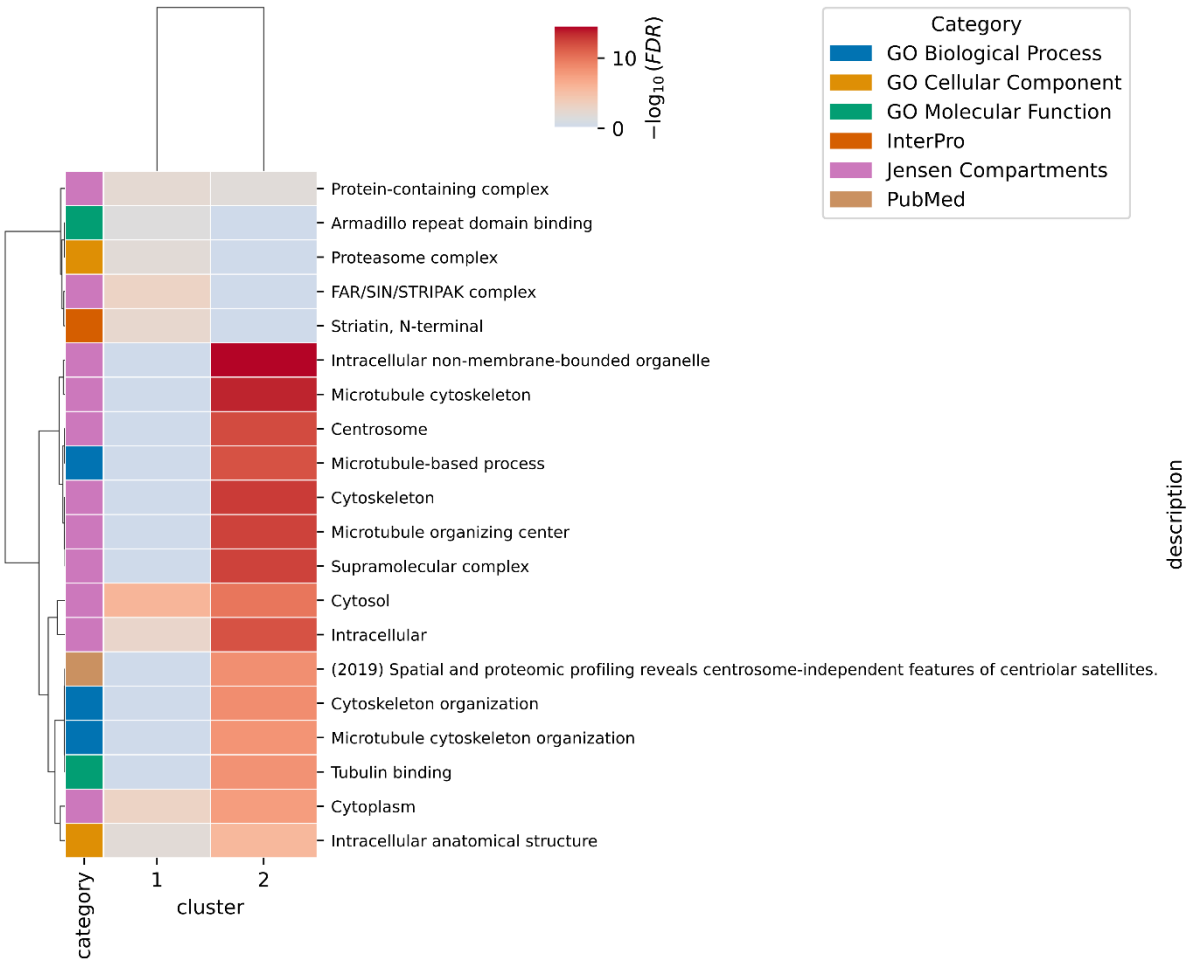

Supplemental Figure 3: heatmap with cluster specific, significantly enriched processes (FDR < 0.01; StringDB) obtained from co-evolution (Jaccard)-based clustering of the LRRK2 BioID interactome.

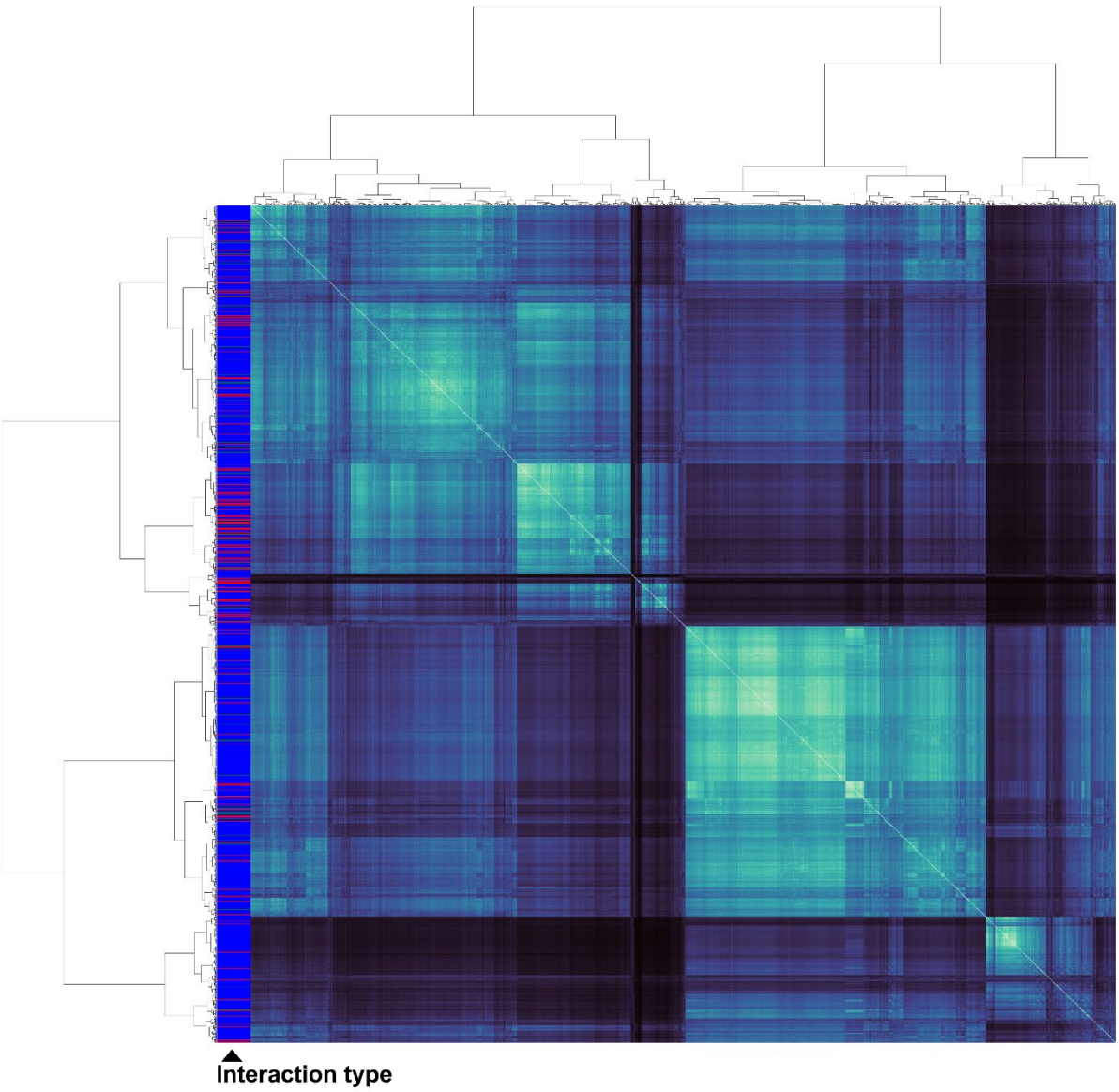

Supplemental Figure 4: heatmap displaying the coevolution (Jaccard)-based hierarchical clustering of the LRRK2's IntAct interactome. Colored bars provide IntAct's interaction type annotation.

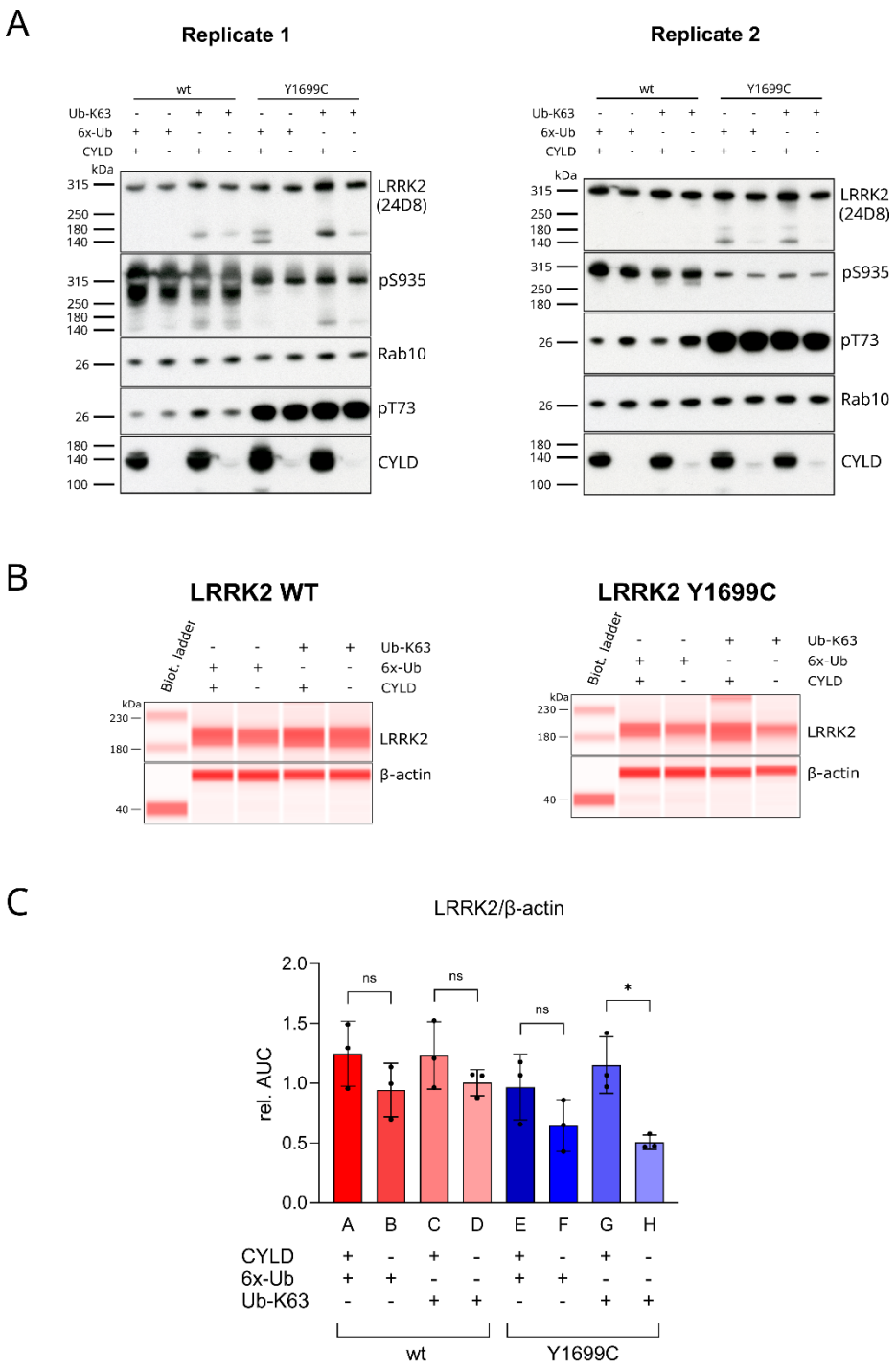

Supplemental Figure 5: Effect of CYLD co-expression on the stability of LRRK2 WT and Y1699C variants. (A) Western blot analysis (ECL detection) of two independent biological replicates. HEK293T cells were transfected with either LRRK2 wild-type (WT) or the Y1699C mutant, co-expressed with CYLD and either a 6xUbiquitin (6xUb) construct or a K63-only ubiquitin mutant (Ub-K63), which restricts polyubiquitin chain formation to K63 linkages. (B, C) Quantification of LRRK2 protein levels from three technical replicates of the second biological replicate (same biological samples analyzed in three independent capillary Western runs), confirming the trend observed in the first replicate (shown in Figure 3). Statistical significance was assessed using unpaired two-tailed t-tests.

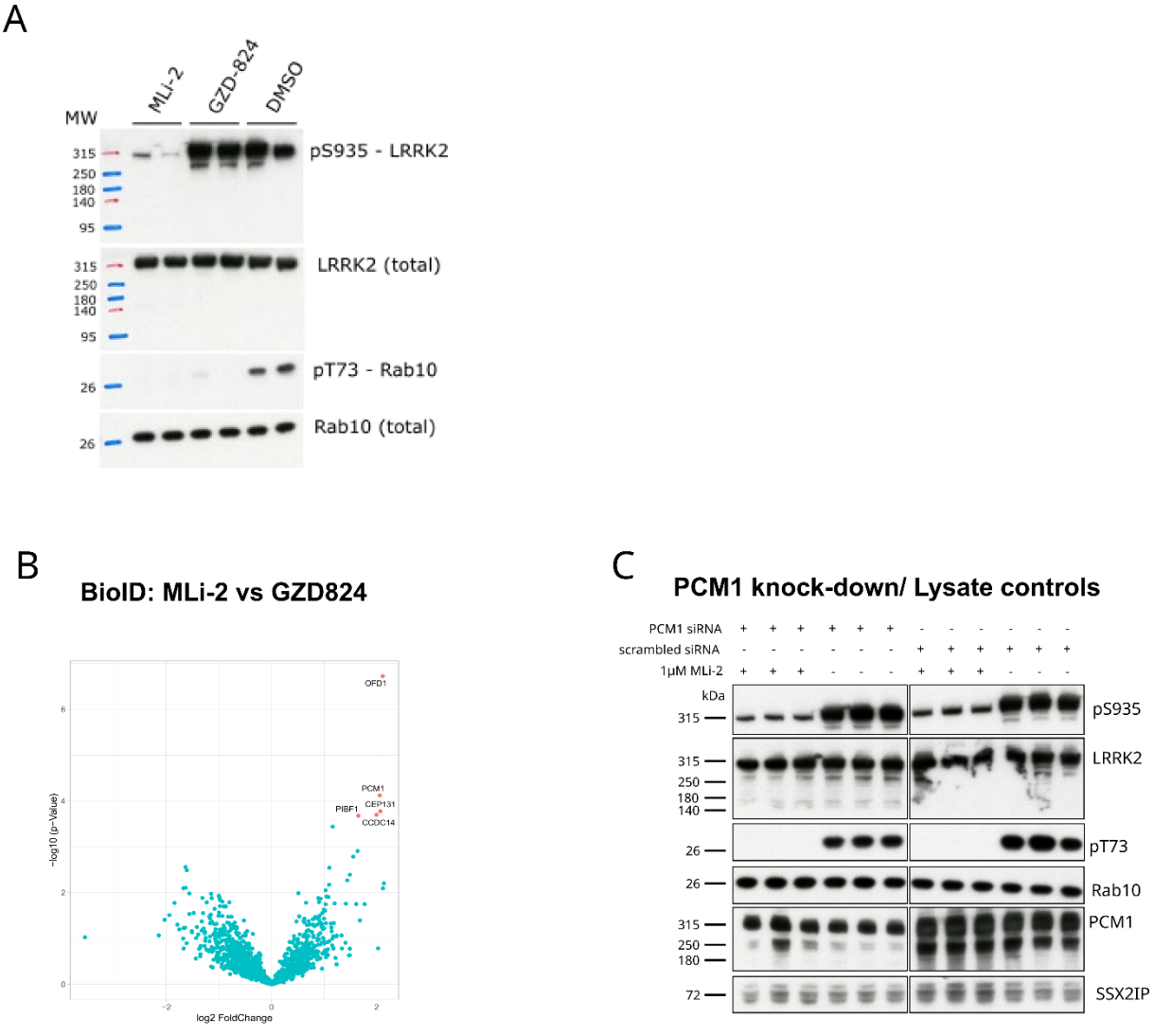

Supplemental Figure 6: (A) Western blot analysis demonstrating effective LRRK2 inhibition by MLi-2 (type I inhibitor) and GZD-824 (type II inhibitor) in HEK293 cells stably expressing miniTurbo-tagged LRRK2. Both compounds at 1 µM significantly reduce Rab10 phosphorylation. As expected, MLi-2 induces a marked loss of LRRK2 pS935 phosphorylation, a hallmark of type I kinase inhibition. In contrast, GZD-824 does not affect pS935 phosphorylation, consistent with its classification as a type II inhibitor(Tasegian et al., 2021). (B) BioID-based proximity labeling comparing the interactome changes upon treatment with MLi-2 versus GZD-824. Volcano plot illustrates differential protein interactions, highlighting the distinct molecular effects of type I and type II LRRK2 inhibition. (C) Validation of PCM1 knock-down by western blot. Efficient depletion of PCM1 is confirmed, with no observed changes in total protein levels of LRRK2, Rab10, or SSX2IP. LRRK2 inhibition by MLi-2 remains effective in the context of PCM1 knock-down.

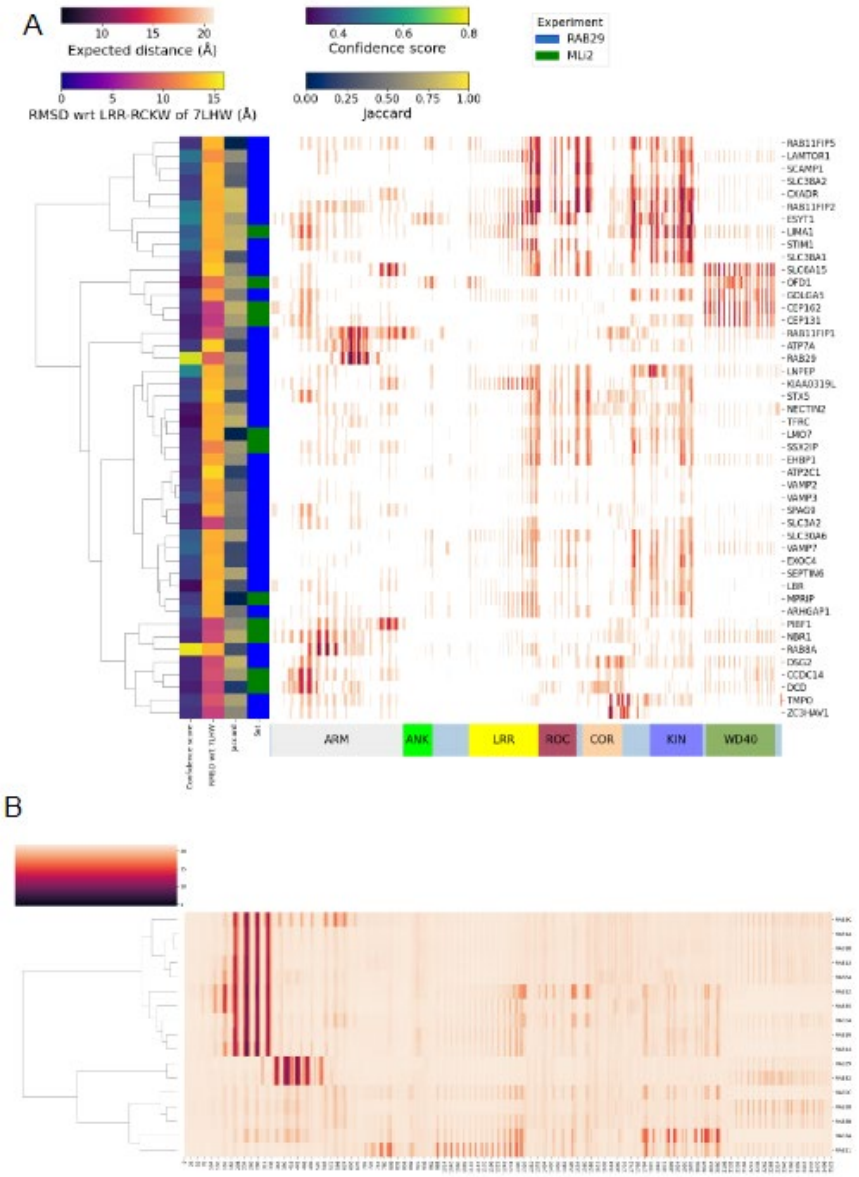

Supplemental Figure 7: (A) interaction fingerprint clustering of LRRK2's modulators (MLi-2 and RAB29) interactomes. Cells contain the minimum expected distance obtained from the distograms of any residue of each interactor (row) to every residue in LRRK2 (column). Rows are color annotated based on confidence score, Jaccard, RMSD from reference LRRK2 structure (PDB: 7LHW) and experiment type (either MLi-2 or RAB29 over-expression); (B) interaction fingerprint of LRRK2 and interacting RABs (from IntAct).